The relationship between lightning activity and ice fluxes in thunderstorms

Wiebke Deierling,[1] Walter A. Petersen,[2] John Latham,[1] Scott Ellis,[1] and Hugh J. Christian[2]

Received 8 December 2007; revised 8 April 2008; accepted 16 April 2008; published 15 August 2008.

[1] It is generally believed that a strong updraft in the mixed-phase region of thunderstorms is required to produce lightning. This is the region where the noninductive charging process is thought to generate most of the storm electrification. Analytic calculations and model results predict that the total lightning frequency is roughly proportional to the product of the downward mass flux of solid precipitation (graupel) and the upward mass flux of ice crystals. Thus far this flux hypothesis has only been tested in a very limited way. Herein we use dual-polarimetric and dual-Doppler radar observations in conjunction with total lightning data collected in Northern Alabama and also Colorado/Kansas during two field campaigns. These data are utilized to investigate total lightning activity as a function of precipitation and nonprecipitation ice masses and estimates of their fluxes for different storm types in different climate regions. A total of 11 storms, including single cell, multicell, and supercell storms, was analyzed in the two climatologically different regions. Time series of both precipitation and nonprecipitation ice mass estimates above the melting level show a good relationship with total lightning activity for the 11 storms analyzed (correlation coefficients exceed 0.9 and 0.8, respectively). Furthermore, the relationships are relatively invariant between the two climate regions. The correlations between total lightning and the associated product of ice mass fluxes are even higher. These observations provide strong support for the flux hypothesis.

Citation: Deierling, W., W. A. Petersen, J. Latham, S. Ellis, and H. J. Christian (2008), The relationship between lightning activity and ice fluxes in thunderstorms, *J. Geophys. Res.*, *113*, D15210, doi:10.1029/2007JD009700.

1. Introduction

[2] Recently, the development and deployment of several ground-based and space-borne lightning detection devices such as the Lightning Imaging Sensor (LIS) [*Christian et al.*, 1999] or the Lightning Mapping Array (LMA) [*Thomas et al.*, 2004] has increased the availability of total lightning measurements significantly. The availability of these data will increase even more dramatically with the deployment of the Geostationary Lightning Mapper (GLM) scheduled for launch on the next generation of Geostationary Operational Environmental Satellites (GOES-R). The availability of continuous total lightning measurements enables us to explore the relationship between lightning flash characteristics/rate and kinematic and microphysical thunderstorm parameters. If robust quantitative relationships between lightning and storm parameters are found, these can be used to incorporate lightning data into several applications, including improved mesoscale model forecasts via added information about convective variables, such as ice water path and latent heating rates; improved definition of the role of convection in the global climate; improvements in Quantitative Precipitation Estimates (QPE), especially in regions with no or poor radar coverage; improved nowcasting of thunderstorm evolution and decay; improved prediction of high societal impact severe weather events such as hail, tornadoes or microbursts; and quantification of lightning-produced Nitrogen Oxides (NO_x) in the mid-upper troposphere.

[3] Numerous field observations have shown clear relationships between both cloud-to-ground and total lightning (cloud-to-ground plus in-cloud) and precipitation ice mass [e.g., *Nesbitt et al.*, 2000; *Petersen and Rutledge*, 2001; *Deierling et al.*, 2005; *Petersen et al.*, 2005a; *Wiens et al.*, 2005; *Latham et al.*, 2007]. Many field observations [*Workman and Reynolds*, 1949; *Williams and Lhermitte*, 1983; *Dye et al.*, 1989; *Rutledge et al.*, 1992; *Carey and Rutledge*, 1996; *Petersen et al.*, 1996, 1999] suggest that a strong updraft in the mixed-phase region (located around 0°C to −40°C) is necessary to produce lightning. This is the region where noninductive charging [*Reynolds et al.*, 1957; *Takahashi*, 1978; *Jayaratne et al.*, 1983; *Williams*, 1989; *Saunders et al.*, 1991; *Saunders*, 1993; *Saunders and Peck*, 1998; *Takahashi and Miyawaki*, 2002; *Mansell et al.*, 2005; *Latham et al.*, 2007] is generally believed to generate most

[1]National Center for Atmospheric Research, Boulder, Colorado, USA.
[2]ESSC/NSSTC University of Alabama in Huntsville, Huntsville, Alabama, USA.

Copyright 2008 by the American Geophysical Union.
0148-0227/08/2007JD009700

of the thunderstorm electrification. Noninductive charging involves rebounding collisions between graupel and ice crystals in the presence of supercooled liquid water. The charge transfer per collision depends on the size of the ice crystals and the fall speed of the graupel pellets, while the sign of the charging depends on temperature and the liquid water content [e.g., *Takahashi*, 1978; *Saunders et al.*, 1991; *Williams et al.*, 1991; *Saunders*, 1993; *Pereyra et al.*, 2000; *Takahashi and Miyawaki*, 2002; *Saunders et al.*, 2006]. Significant charging occurs only where graupel, ice crystals and supercooled droplets co-exist. This region is referred to as the "charging zone" and its vertical extent is limited [e.g., *Latham et al.*, 2004]. The upper limit of the charging zone is the level above which these three types of hydrometeor do not coexist. The larger the updraft speed, the higher this diffuse threshold will extend. The upper boundary typically lies between the −15°C and −30°C isotherms [e.g., *Latham et al.*, 2004], and it is likely that most of the charging crucial to lightning production occurs just below it. This is principally because the charge transfer per collision increases rapidly with larger crystal sizes [*Keith and Saunders*, 1990]. Also, crystals may be more numerous at the top of the charging zone. The lower boundary of the charging zone is also diffuse and dependent upon the prevailing glaciation mechanism, but can characteristically be taken to be a few degrees colder than 0°C.

[4] Based on these ideas, analytic calculations by *Blyth et al.* [2001] and *Latham et al.* [2004] yielded the prediction that the lightning rate (f) is roughly proportional to the product of the downward flux (p) of solid precipitation (graupel) and the upward mass flux (F_i) of ice crystals, the values of p and F_i being those existing at the top of the charging zone. Here p is the product of precipitation ice mass (p_m) and the terminal fall speed of hydrometeors (v_t) and F_i is the product of nonprecipitation ice mass (np_m) multiplied by the vertical wind speed (w). In the following, this prediction of a proportionality between lightning rate and flux product will be referred to as the flux hypothesis. The predicted equation valid in the charging zone that describes the flux hypothesis is

$$f = C \cdot p \cdot F_i,$$

where C is a constant, $p = p_m \cdot v_t$ and $F_i = w \cdot np_m$.

[5] Initial support for the flux hypothesis was provided computationally, using multiple lightning activity models [*Baker et al.*, 1995, 1999]. More recent modeling and observational studies also suggest a good correlation between total lightning rate and flux product components such as graupel volume, the updraft volume and the updraft mass flux for at least one severe thunderstorm case simulated [*Wiens et al.*, 2005; *Kuhlman et al.*, 2006]. Nevertheless to date there has been only limited preliminary observational evidence for the flux hypothesis [*Deierling et al.*, 2005].

[6] The goals of this study are to examine observational evidence (based on ground-based polarimetric radar and lightning measurements) on a storm scale for a variety of storm types and environments to test and, if justifiable, quantify the flux hypothesis, and to investigate and refine Tropical Rainfall Measurement Mission (TRMM) observations that indicate a global relationship between averaged precipitation ice mass water content and total lightning activity [*Petersen et al.*, 2005a] on a storm scale. A verified and robust general relationship of $f = C \cdot p \cdot F_i$ that is valid on storm as well as large-scale averages may enable us to

- estimate (solid) thunderstorm precipitation in remote areas, and
- estimate ice mass contents lofted into and detrained from thunderstorm anvils
- parametrize lightning activity via the ice mass fluxes in climate, meso- and cloud scale models to estimate other properties such as NO_x production.

[7] Section 2 gives an overview of the data used in this analysis. In section 3, methodologies for observing and computing precipitation and nonprecipitation ice masses and their fluxes from polarimetric radar data are described. Section 4 presents observational results describing the relationship between ice masses and their fluxes and total lightning. Section 5 provides a summary of the observationally diagnosed relationship between total lightning, ice mass and ice fluxes, and the possible utilization of these relationships on storm scales.

2. Data

[8] To investigate the flux hypothesis, polarimetric radar and total lightning data collected in Northern Alabama during 2005 were used as well as data from two field projects that took place in the High Plains of Colorado/Kansas: one is the Stratospheric-Tropospheric Experiment: Radiation, Aerosols and Ozone (STERAO-A) [*Dye et al.*, 2000], the other one the Severe Thunderstorm Electrification and Precipitation Study (STEPS) [*Lang et al.*, 2004]. A list of thunderstorms that have been investigated in this study, including a short description of the storms, is given in Table 1. Note that not all storms could be observed throughout their entire lifetime, since some storms moved in or out of the observational domain. Herein a storm can consist not only of one but several cells (e.g., multicells) but is otherwise separated from surrounding storms if they exist.

[9] During the STERAO-A project, total lightning activity was recorded by the Office Nationale d'Etudes et de Recherches Aerospatiales (ONERA) three-dimensional lightning VHF-interferometer system [*Defer et al.*, 2001; *Laroche et al.*, 1994]. Dual-polarimetric radar data were collected from the Colorado State University-University of Chicago-Illinois State Water Survey (CSU-CHILL) National Radar Facility's S-band radar [*Brunkow et al.*, 2000] over the ONERA interferometer coverage domain. Thus the lightning interferometer data could be placed within the context of storm-scale kinematic and microphysical environments.

[10] During STEPS total lightning activity was detected by the deployable Lightning Mapping Array (LMA) of the New Mexico Institute of Mining and Technology (NMIMT) [*Thomas et al.*, 2004]. The CSU-CHILL and the NCAR S-band dual-polarimetric (S-Pol) radars provided dual-polarimetric radar data. These two research radars together with the Goodland, Kansas National Weather Service (NWS) Weather Surveillance Radar-1988 Doppler (WSR-88D) radar formed a triangle with approximately 60 km

Table 1. List of Thunderstorms That Have Been Investigated in This Study

Date	Project	Storm Type	Number of Investigated Storms	Short Description
21 February 2005	Northern Alabama	Severe storm, multicellular character	1	Several hail reports of 1.8 to 2.3 cm hail from SPC[a]
7 April 2005	Northern Alabama	Moderate intensity ordinary thunderstorm, approaching severe	1	Hail report of 1.8 cm hail from SPC
13 July 2005	Northern Alabama	Single cell thunderstorms	3	No hail, wind, or tornado reports
10 July 1996	STERAO-A	One multicell storm evolving to a supercell storm [*Dye et al.*, 2000]	1	No large hail or strong winds reported
6 June 2000	STEPS	Single cell thunderstorms	3	No hail, wind, or tornado reports
5 July 2000	STEPS	Supercell thunderstorms [*Lang et al.*, 2004; *MacGorman et al.*, 2005]	2	One supercell had a funnel cloud, hail reports of 2.5 and 4.3 cm hail from SPC and 33 m/s gusts [*Lang et al.*, 2004]

[a]SPC = Storm Prediction Center Reports from the National Oceanic and Atmospheric Administration (NOAA) and the National Weather Service (NWS).

baselines and performed synchronized volume scans allowing dual- or triple-Doppler wind analysis.

[11] Ground-based total lightning data in conjunction with polarimetric radar and sounding data have been available from storms occurring in Northern Alabama since the end of 2004 and are well suited for this study. For storm cases in Northern Alabama, total lightning data were collected by the North Alabama Lightning Mapping Array, which is permanently installed in the Huntsville, AL area [*Goodman et al.*, 2005]. It is a very similar system to the LMA deployed during STEPS and consists of 10 stations. Polarimetric radar data were collected from the University of Alabama Huntsville/National Space Science and Technology Center (UAH/NSSTC) C-band ARMOR radar (Advanced Radar for Meteorological and Operational Research) [*Petersen et al.*, 2005b]. For cases examined in this study, the ARMOR radar was operated in Simultaneous linear Transmit And Receive (STAR) mode. In this mode the radar reflectivity (Z), radial velocity (V_r), spectrum width (SW), differential reflectivity (ZDR), correlation coefficient (ρ_{hv}) and differential phase (Φ_{DP}) were collected. Only the linear depolarization ratio (LDR) (which is collected from CHILL and SPOL) cannot be measured in this mode. C-band radars suffer from strong attenuation in observations of heavy rain or large hail. Thus the reflectivity and the differential reflectivity fields measured by ARMOR were corrected for attenuation and differential attenuation, respectively, using a self-consistent constrained "ZPHI" approach [*Testud et al.*, 2000; *Bringi et al.*, 2001; *Petersen et al.*, 2005b]. The ARMOR radar and the nearby Hytop WSR-88D radar allow dual-Doppler wind retrievals under the coverage umbrella of the North Alabama LMA.

[12] Thermodynamic data, specifically temperature profiles, were retrieved from sounding data collected in both field campaigns and from operational soundings in the Northern Alabama region (e.g., Birmingham and Nashville soundings from the National Weather Service).

3. Methodology

3.1. Determination of Lightning Flashes From VHF Sources

[13] Lightning flashes consist of various electric current segments that emit electromagnetic radiation over a broad band. Some components of a lightning flash emit strongly in the VHF frequency domain, namely breakdown processes, recoil streamers, negative stepped leaders, dart leaders and sometimes return strokes. Other components, such as positive leader processes, emit much less VHF radiation [see *Shao et al.*, 1999]. These emission characteristics are important for proper interpretation of measurements from both the ONERA lightning interferometer and the LMA systems.

[14] For the STERAO-A case (10 July 1996 storm) the process of integrating related VHF sources (in time and space) detected by the ONERA lightning mapper to produce discrete lightning flashes was performed by *Defer et al.* [2001]. They used an automated algorithm to group VHF sources to flash components and flash components to a flash by applying temporal and spatial constraints. In addition to determine a flash they used what they termed angular analysis. Here, an operator uses azimuth, elevation and magnitude information of measured VHF sources from individual ONERA lightning mapper stations to determine whether or not VHF sources belong to the same flash. Only one time criterion was applied; a VHF source was assigned to a new flash if it was recorded 0.5 s after the occurrence of the last source. As the information from both stations was considered individually, sources detected by one station and not by the other were also taken into account. Single sources with a time duration of 23 μs (which is the time resolution of the system) were allowed to count as one flash if they did not appear to be linked to another source.

[15] For both the STEPS and Northern Alabama LMA data, flashes were determined from VHF sources using two methods. Prior to discussing the specifics of the flash algorithms it is worth noting that in both LMA systems a given VHF source in a lightning flash was not counted unless at least seven stations detected the source. This seven-station detection threshold reduces the number of noise contaminated sources from interference, which occurs in the Northern Alabama area and during one STEPS case. However it is also possible that valid (low power) VHF sources emitted by lightning could have been eliminated [*Thomas et al.*, 2004]. The first method to determine flashes from measured VHF sources was to use the flash algorithm built into the LMA software [*Thomas et al.*, 2003]. The algorithm applies user specified temporal and spatial conditions for VHF sources to be attributed to the same flash. For this study we required that sequential VHF sources could not be separated by more than 150 ms in time, 3 km in horizontal distance and 5 km in the vertical [*Thomas et al.*,

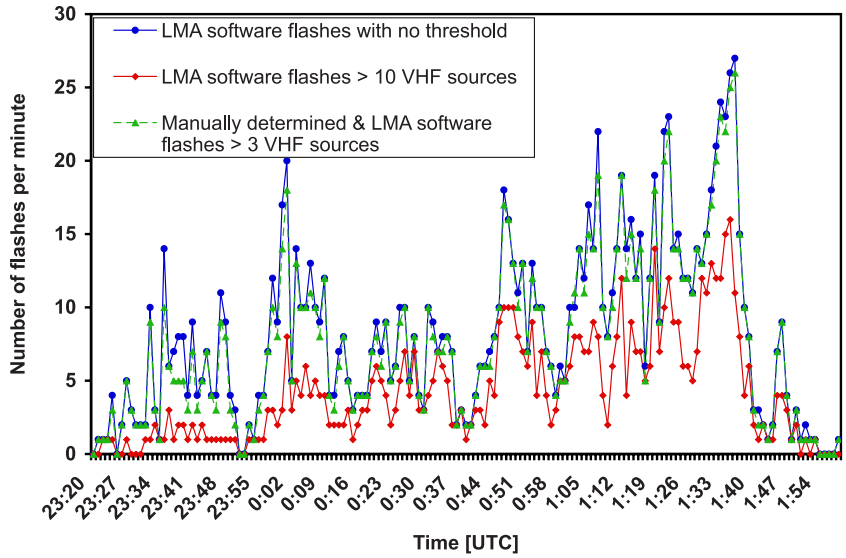

Figure 1. Lightning flash rates retrieved from the flash algorithm built into the LMA software showing nonthresholded flashes (solid blue line), thresholded flashes greater than 10 VHF sources (solid red line), and flashes determined by the author (dashed green line) of an ordinary thunderstorm that occurred on 6 June 2000 during STEPS. Thresholded flashes with more than three VHF sources were nearly identical (with one exception) to the ones identified by the author and also represented by the green dashed line.

2003; *Wiens et al.*, 2005]. Furthermore, the LMA software allows users to specify the minimum number of VHF sources that constitute a flash. Total flash rates with a minimum of 1, 3, and 10 VHF sources were calculated to investigate the influence on flash rate trends. As an example, Figure 1 shows flash rates computed using a minimum of 1, 3, and 10 VHF sources for an ordinary thunderstorm that took place during STEPS on 6 June 2000. For this example as well as in other thunderstorms with low to moderate lightning activity, it was found that the overall trend of the flash rates remain consistent, even though the total number of flashes decreases with a higher minimum of VHF sources constituting a flash. This result is also consistent with the findings of *Wiens et al.* [2005].

[16] The second method to determine flashes, similar to the angular analysis performed by *Defer et al.* [2001], was performed manually and used for low and moderate flash rates. Following *Defer et al.* [2001] flashes were identified looking at consecutive 3 s time windows and combining VHF sources into components using their (x,y,z) information and time displayed by the LMA software. Single VHF sources with of time duration of 80 μs (equal to the time resolution of the LMA) were allowed to count as a flash. This analysis was performed for most of the analyzed storms with the exception of two supercell storms on 5 July 2000 (during STEPS) and for the 21 February 2005 storm that took place in Northern Alabama. Here the lightning rate was too high to objectively determine flashes manually, in agreement with *Wiens et al.* [2005].

[17] The manually determined flash frequencies were compared to flash frequencies from the LMA software algorithm. The results demonstrate that for low and moderate flash rates, flash rates determined manually were nearly identical to those calculated by the built in flash algorithm from the LMA software using a minimum of three sources to constitute a flash (Figure 1). Flash rates allowing one VHF source to constitute a flash may lead to unreasonably high flash rates, especially for storms with a high lightning activity as some of these sources may be due to noise [*Thomas et al.*, 2003; *Wiens et al.*, 2005]. To remain consistent with the STERAO-A analysis and because short duration flashes (flashes with a duration less than 1 ms) can occur [*Thomas et al.*, 2003; *Defer et al.*, 2001], flash rates determined with the operator analysis were used in this study whenever possible. For the 5 July 2000 and 21 February 2005 cases flash rates determined with the built in flash algorithm from the LMA software were used allowing a minimum of three VHF sources to constitute a flash.

3.2. Ice Mass Flux Computations From Dual-Polarimetric Doppler Radar Data

[18] In order to compute the ice mass flux product in the charging zone and examine the flux hypothesis, estimates of the following are required: Precipitation ice mass, non-precipitation ice mass, and information about the three dimensional wind field of a thunderstorm. Herein, the first step was to identify bulk microphysical hydrometeor types from the polarimetric radar data [e.g., *Vivekanandan et al.*, 1999; *Straka et al.*, 2000; *Liu and Chandrasekar*, 2000; *Zrnic et al.*, 2001]. This was accomplished with the National Center for Atmospheric Research (NCAR) fuzzy logic Particle IDentification algorithm (PID) [*Vivekanandan et al.*, 1999]. The NCAR PID operates in radar space (spherical coordinate system) and uses nine input variables: radar reflectivity, differential reflectivity, linear depolarization ratio, correlation coefficient, specific differential phase, a temperature profile, standard deviation of velocity, standard deviation of differential reflectivity and standard deviation of the differential phase to distinguish between 17 output categories. The temperature profiles used for the PID

Table 2. Z-M Relationships for Various Hydrometeor Types, Where M is in (g/m^3) and Z in (mm^6/m^3)

Hydrometeor Categories	NCAR PID Categories	Z-M Relationship	Reference
Nonprecipitation ice	Dry snow, oriented ice, irregular ice	$M = 0.017 \cdot Z^{0.529}$	*Heymsfield and Palmer* [1986]
Precipitation ice: graupel	Graupel/small hail, graupel/small hail/rain mixture	$M = 0.0052 \cdot Z^{0.5}$	*Heymsfield and Miller* [1988]
Precipitation ice: hail	Hail, hail/rain mixture	$M = 0.000044 \cdot Z^{0.71}$	*Heymsfield and Miller* [1988]

originate from soundings made during STERAO-A and STEPS close to the storms and from the NWS for the Northern Alabama region as described in section 2. The output categories of the NCAR PID are: cloud droplets, drizzle, light rain, moderate rain, heavy rain, hail, hail/rain mix, graupel/small hail, graupel/small hail/rain mix, dry snow, wet snow, irregular ice crystals, horizontally oriented ice crystals, super cooled liquid drops, insects, second trip, and ground clutter. To relate the microphysics data to a 3D wind field on a Cartesian grid the PID output, temperature and radar reflectivity were gridded with the NCAR/EOL software package REORDER using a closest point weighting scheme. Once the precipitation ice and nonprecipitation ice regions were identified with the PID (see below) and converted to a Cartesian grid, the mass contents were then estimated using reflectivity (Z) - mass content (M) relationships of the kind $M = aZ^b$ from the literature [e.g., *Sassen*, 1987]. The 3D wind field was estimated from dual-Doppler retrievals using NCAR's Custom Editing and Display of Reduced Information in Cartesian space (CEDRIC) [*Mohr et al.*, 1986] software package. A detailed description of the dual-Doppler synthesis performed herein is given by *Deierling and Petersen* [2008]. In one case, data from only one radar was available and the three-dimensional wind field was determined using NCAR's Variational Doppler Radar Assimilation System (VDRAS) [*Sun and Crook*, 1997, 2001; *Crook and Sun*, 2004].

[19] To better facilitate the observational study of the flux hypothesis using the PID hydrometeor classifications, some particle types were reduced to two general classes: precipitation and nonprecipitation ice. In this study, PID categories of hail, hail/rain mix, graupel/small hail and graupel/small hail/rain mix above the height of the −5°C level were combined to represent precipitation ice in the charging zone (Table 2). Then the precipitation ice mass was calculated in Cartesian space. For PID graupel/small hail and graupel/small hail/rain mix and hail, hail/rain mix their ice mass contents was calculated in each grid of a given radar volume using Z-M relationships from *Heymsfield and Palmer* [1986] and *Heymsfield and Miller* [1988], respectively (Table 2) and multiplied by the grid volume to obtain ice mass. Precipitation ice mass fluxes were calculated at each grid point multiplying the ice mass with calculated particle fall speeds. Particle fall speeds (v_t) for precipitation ice were determined using the $v_t - Z$ relationships $v_t = 0.817 \cdot Z_h^{0.063}$ from *Marks and Houze* [1987]. Storm total precipitation ice mass and ice mass fluxes were obtained calculating the sum of the ice mass or ice mass flux values in the individual grid points of a given radar volume. Note, that we do not account for fractions of rain for the grid points that are identified as precipitation ice/rain mix. The rain fractions make a part of the reflectivity that is used to compute the precipitation ice mass. However, it was investigated whether this had any significant impact on the computation of the precipitation ice mass. It was found that assuming the most extreme (and unrealistic) liquid/ice reflectivity fraction had very little impact on the overall result, i.e., assuming all of the mixed-phase reflectivity comes from liquid and therefore eliminating the entire mixed-phase region from the ice mass computations. As an example the linear fit for total lightning an precipitation ice mass without the mixed-phase categories is $f = 3.4 \cdot 10^{-8} p_m - 15$, the linear fit for total lightning and precipitation ice including the mixed-phase categories is very similar: $f = 3.4 \cdot 10^{-8} p_m - 18$ (see Table 6).

[20] Due to dependence of the radar power measurements on the sixth power of particle diameter, the radar primarily detects the largest particles present in a given pulse volume. Therefore small ice crystals mixed with larger graupel or hail will go undetected and estimates of nonprecipitation ice mass have to be made in absence of direct measurements. Herein, two approaches were employed to compute a representative quantity for nonprecipitation ice mass:

[21] 1. Nonprecipitation ice mass estimate (temperature threshold): PID categories of dry snow, irregular ice crystals and horizontally oriented ice crystals above a temperature level (−50°C), near the top the storm, with reflectivity values below 20 dBZ were used as a proxy to represent advected nonprecipitation ice mass that originated in the charging zone. This nonprecipitation ice mass estimate will be referred to as NPIM_T in the following. The temperature level was used as a proxy to include ice mass transported into the thunderstorm anvil that represents nonprecipitation ice mass created lower in the cloud in the mixed ice phase region. Similar to precipitation ice mass calculations, nonprecipitation ice mass contents were calculated (in Cartesian space) in each grid containing the PID categories listed above using the Z-M relationship from *Heymsfield and Palmer* [1986] (see Table 2). Storm total ice masses were calculated by first multiplying individual grid ice mass contents with the grid volume and then summing all ice masses over the radar volume.

[22] 2. Nonprecipitation ice mass estimate (divergence method): PID categories of dry snow, irregular ice crystals and horizontally oriented ice crystals above the temperature level of −5°C with divergence values larger than 0.001 s^{-1} and reflectivity values below 20 dBZ were chosen to represent nonprecipitation ice from the charging zone. This will be referred to as NPIM_DIV in the following. Nonprecipitation ice mass storm totals were calculated as described in the first estimate using Z-M relationship from *Heymsfield and Palmer* [1986]. Utilizing the divergence to identify nonprecipitation ice exiting the updraft originates with the assumption that the anelastic continuity equation is satisfied (horizontal density changes are ignored but density changes with altitude are allowed) given by

$$\nabla_H \rho_0 V = \partial(w\rho_0)/\partial z, \quad (1)$$

where ρ_0 is the base state density and a function only of height, w is the vertical velocity, V is the horizontal velocity

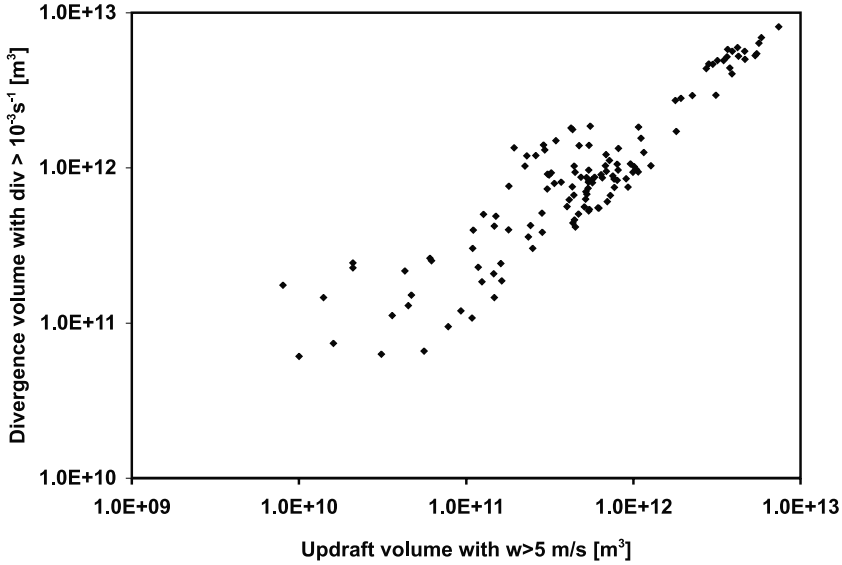

Figure 2. Total storm volumes with vertical velocity above 5 m/s above the −5°C level versus total storm volumes with horizontal divergence >0.001 s^{-1} above the −5°C level from all investigated thunderstorm cases. The correlation coefficient has a value of 0.96 between the divergence and vertical velocity volumes.

and z the vertical depth. According to equation (1), the horizontal mass divergence (left side) is equal to the change of vertical mass flux with height (right side), assuming also that w = 0 m/s at the top of the thunderstorm and at the surface. Thus, at a given level, an increase in w with height is expected to be accompanied by horizontal convergence, a decrease in w with height by horizontal divergence. This leads to the assumption of low-level mass convergence below the maximum in w and upper-level mass divergence above the maximum in w [e.g., *Witt and Nelson*, 1991; *Yuter and Houze*, 1995]. The assumption here is that the upper-level horizontal divergence above a threshold can be used to approximate nonprecipitation ice mass exiting the updraft. Importantly the divergence threshold also limits the area of nonprecipitation ice surrounding the updraft included in each radar volume. This is important in order not to include the long-lived anvil ice mass in the estimation of the nonprecipitation ice mass flux.

[23] The divergence herein was calculated using the horizontal wind components from the dual-Doppler synthesis or VDRAS. An appropriate divergence threshold would result in a volume similar to the total updraft volume in the charging zone. To determine this threshold we compared updraft volumes with vertical velocities greater than values varying from 1 to 5 m/s to divergence volumes with varying thresholds. It was found that calculated total storm volumes of vertical velocities greater than 1–5 m/s correspond best to total divergence volumes greater than 0.001 s^{-1} in most investigated cases. As an example, Figure 2 shows a scatterplot of total storm volumes above the −5°C level with vertical velocities above 5 m/s versus total storm volumes above the −5°C level with divergence greater than 0.001 s^{-1} including data from all investigated thunderstorm cases. The correlation coefficient between the divergence and vertical velocity volumes has a value of 0.96, suggesting a strong relationship between the two. Thus the divergence threshold 0.001 s^{-1} was chosen in this study.

[24] To compute estimates of the nonprecipitation ice mass flux (F_i), NPIM_DIV (divergence method nonprecipitation ice mass estimate) was multiplied by the horizontal divergence in each grid and then summed over the storm volume. The product ($p{\cdot}F_i$) of storm total precipitation and nonprecipitation ice mass fluxes per radar volume were then obtained and could be compared to the total lightning rate in order to test the flux hypothesis.

[25] To verify the nonprecipitation ice mass flux estimate (product of divergence and nonprecipitation ice colder than −5°C with reflectivities smaller than 20 dBZ and with divergence greater than 0.001 s^{-1}), it was tested with model output from a storm simulation with the Weather Research and Forecasting (WRF), Version 2.2 [e.g., *Wicker and Skamarock*, 2002; *Skamarock et al.*, 2005]. Three-dimensional dynamic models such as WRF can resolve the microphysical and dynamic structure of simulated thunderstorms including nonprecipitation ice inside and outside the thunderstorm updraft regions. The purpose of the simulation was not to reproduce a particular storm with the WRF model, but only to test the methodology used for the calculation of the nonprecipitation ice flux estimate. This was accomplished by using the model output to compute the flux estimate with divergence method and compare it to the nonprecipitation ice mass flux in the updraft region of the simulated thunderstorm.

[26] Simulations were performed with *Lin et al.*'s [1983] single moment microphysics scheme with horizontal grid spacing of 1 km. In the model the mixing ratios of water vapor, cloud water, rain, cloud ice, snow and graupel are predicted and the radar reflectivity factor Z was calculated from the sum of reflectivities over all hydrometeor species using Rayleigh theory as described by *Ferrier* [1994]. The model simulation is similar to that of the 10 July 1996

Table 3. Thunderstorm Characteristics of the Observed 10 July 1996 Thunderstorm and a Modeled Thunderstorm Using the WRF Model [*Skamarock et al.*, 2000, 2003]

	Modeled Thunderstorm	Observed Thunderstorm
Thunderstorm height, km	~13	14–15
Thunderstorm width, km	~80	~60–90
Maximum radar reflectivity, dBZ	peaks ~ 55 for multicell peaks ~ 70 for supercell	peaks ~ 60 for multicell peaks ~ 63 for supercell
Maximum updraft speed, m/s	25–50	25–38

STERAO storm described by *Skamarock et al.* [2000, 2003] and *Barth et al.* [2007]. After the spin up time of the model, the simulated mature stage storm characteristics (maximum updraft speed, maximum reflectivity, storm width and height) were compared with the observed storm occurring on 10 July 1996. The simulated storm has in its first stage a multicellular character transitioning to a supercell at the end of its lifetime as it is observed. Some further storm characteristics of the modeled and observed thunderstorm are listed in Table 3. Thunderstorm height, width, maximum reflectivity and maximum updraft speed compare fairly well between the simulation and the observations. This is also true for the time series of updraft volumes of w > 5m/s and graupel as well as nonprecipitation ice masses above −5°C (not shown). Nonprecipitation ice in the model is taken to be ice categories of ice crystals and snow (with fall velocities < updraft speed).

[27] To test the nonprecipitation ice mass flux estimate from observations used in this study with the model output, first the nonprecipitation ice mass flux above −5°C was calculated as the product of updraft velocity and mixing ratio of the sum of pristine ice and snow mixing ratios (with fall velocities < updraft speed) with radar reflectivities below 20 dBZ above the −5°C level. In a second step, the nonprecipitation ice mass flux was calculated similar to the observations as the product of horizontal divergence and the mixing ratio of the sum of pristine ice and snow mixing ratios (above the −5°C level and with divergence greater than 0.001 s^{-1}). Figure 3 shows the scatterplot of the modeled nonprecipitation ice mass flux and the estimate. The correlation coefficient between the two is 0.91. The result indicates that the nonprecipitation ice mass flux estimated with the divergence method is 1–2 orders of magnitude less but the trend between the two is very similar. Figure 4 shows the time series from the nonprecipitation ice mass flux estimate from the observations overlaid with the nonprecipitation ice mass flux and its estimate calculated from the model data. It can be seen that the trends of all shown fluxes are fairly similar. Note, that similar results were obtained with model results from a RAMS simulation of the 21 February 2005 storm [*Deierling*, 2006].

[28] From these model simulation results we conclude that the nonprecipitation ice mass flux estimate used in this study may be taken as a rough estimate for the nonprecipitation ice mass flux in the charging zone.

3.3. Sensitivity Studies of Mass Computations

[29] Sensitivity studies of nonprecipitation and precipitation ice mass calculations using different Z-M relationships from the literature, different grid scales with applicable radius of influence and different membership functions of the PID dry snow and graupel/small hail categories will be

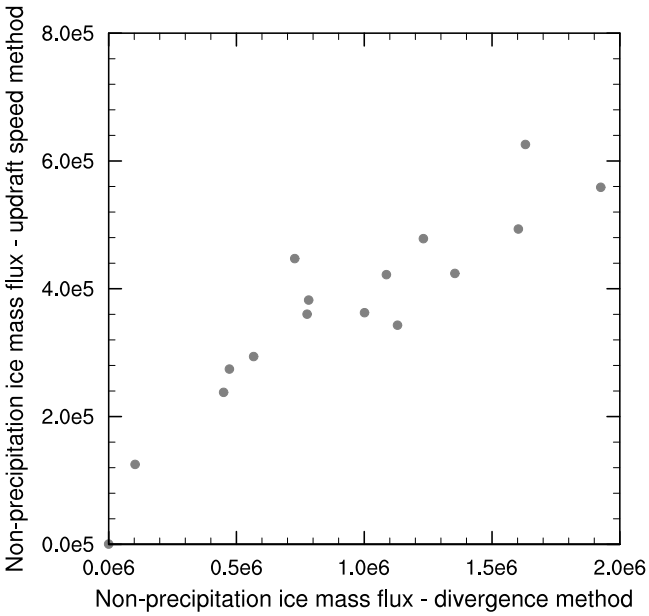

Figure 3. Scatterplot of the nonprecipitation ice mass flux computed with the divergence method from a model simulation versus the directly computed nonprecipitation ice mass flux (updraft speed method) from the same model simulation of the 10 July 1996 storm, courtesy of Christelle Barthe.

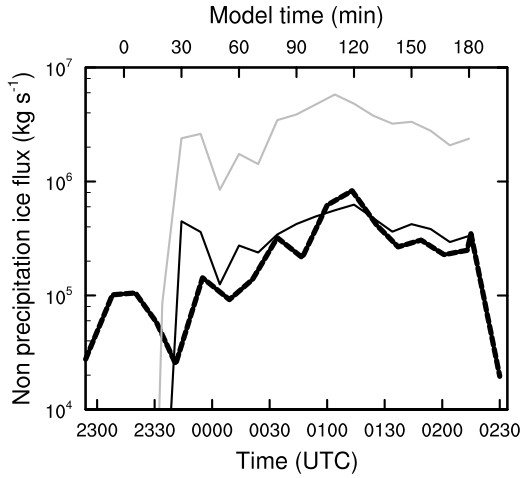

Figure 4. Time series of the nonprecipitation ice mass flux for the 10 July STERAO storm from the observations (black thick line). The simulated ice mass flux using WRF has been computed with two different methods: the divergence method (black thin line) and the directly computed ice mass flux (gray thin line), courtesy of Christelle Barthe.

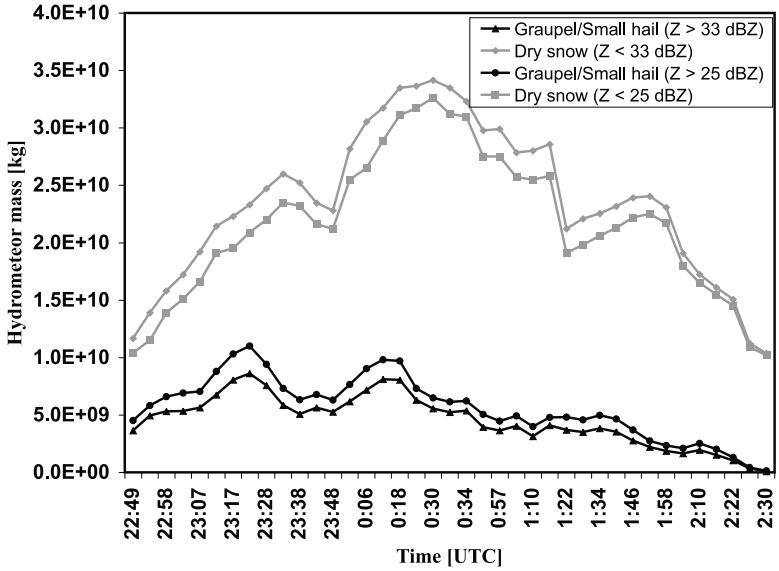

Figure 5. Time series of storm total dry snow mass and graupel/small hail mass above the −5°C level using two versions of PID membership functions for the 10 July 1996 STERAO-A storm. The first version of the PID membership function for dry snow and graupel/small hail overlapped at a reflectivity value of 33 dBZ, the second one overlapped at 25 dBZ. The ice masses were calculated in radar space using Z-M relationships from *Heymsfield and Palmer* [1986] and *Heymsfield and Miller* [1988] for dry snow and graupel/small hail categories, respectively.

investigated in the following to see how robust the computed ice mass trends are.

3.3.1. Sensitivity Studies Between Membership Functions of Dry Snow and Graupel

[30] The PID dry snow category, which represents snow aggregates and crystals, is a component of nonprecipitation ice in this study and the graupel/small hail category is the major component of precipitation ice. The dry snow category contains the highest reflectivity values in the nonprecipitation ice category and thus can have a significant impact on mass computations using power law Z-M relationships. Microphysical distinctions between aggregates, in particular when they start riming, and graupel pellets are somewhat diffuse [*Pruppacher and Klett*, 1997]. Distinguishing between graupel and snow aggregates from polarimetric radar data is also very difficult as their polarimetric radar signatures partly overlap. There are some conflicting values of radar data for graupel and dry snow reported in the literature. For example, low-density graupel may be associated with reflectivity values as low as 20 dBZ according to *Straka et al.* [2000] whereas *Doviak and Zrnic* [1993] allow graupel/small hail to occur only at reflectivities larger than 45 dBZ. Therefore sensitivity studies were performed to see how changes of the PID fuzzy membership functions within the region of overlapping radar signatures affect the trend of dry snow and graupel/small hail mass using the Z-M relationships of *Heymsfield and Palmer* [1986] and *Heymsfield and Miller* [1988], respectively. Membership functions are designed to represent the degree to which the input variable belongs to each of the appropriate outputs, or particular particles [*Vivekanandan et al.*, 1999]. They are piecewise linear and vary between 0 and 1, with 0 indicating the input does not belong to the output and 1 indicating the input has the highest degree of membership.

[31] The largest differences between mass trends were found for the following two versions of membership functions for dry snow and graupel/small hail. In the first version, the boundary of the dry snow reflectivity membership functions started at 35 dBZ with a value of zero following *Doviak and Zrnic* [1993] and *Straka et al.* [2000]. They then increased linearly to a value of one at 33 dBZ. The graupel/small hail reflectivity membership function was zero below 31 dBZ and increased linearly to a value of one at 33 dBZ (the transition reflectivity value). For the second version, which we used in this study, the transition reflectivity value between the dry snow and graupel/small hail categories was lowered to 25 dBZ and the linear slopes of the membership functions remained constant so that they reached a value of zero 2 dB above/below the transition reflectivity value (for dry snow and graupel/small hail, respectively). Thus the dry snow reflectivity membership functions started at 27 dBZ with a value of zero and increased linearly to a value of one at 25 dBZ. The graupel/small hail function was zero at 27 dBZ and increased linearly to a value of one at 29 dBZ.

[32] For the 10 July 1996 STERAO-A storm, Figure 5 shows the differences in the time series between the storm total mass of dry snow and graupel/small hail above the −5°C level (because we are only concerned with the mass colder than this temperature) calculated with the two versions of the membership functions. The trends of the time series for the two versions of graupel/small hail and dry snow are very similar though the actual mass content values vary slightly. The correlation coefficient between the time series of the two versions for the individual categories is above 0.99 in both cases. Thus the sensitivity of the trend to reasonable changes in membership function boundaries is very small and the separation of dry snow and graupel is

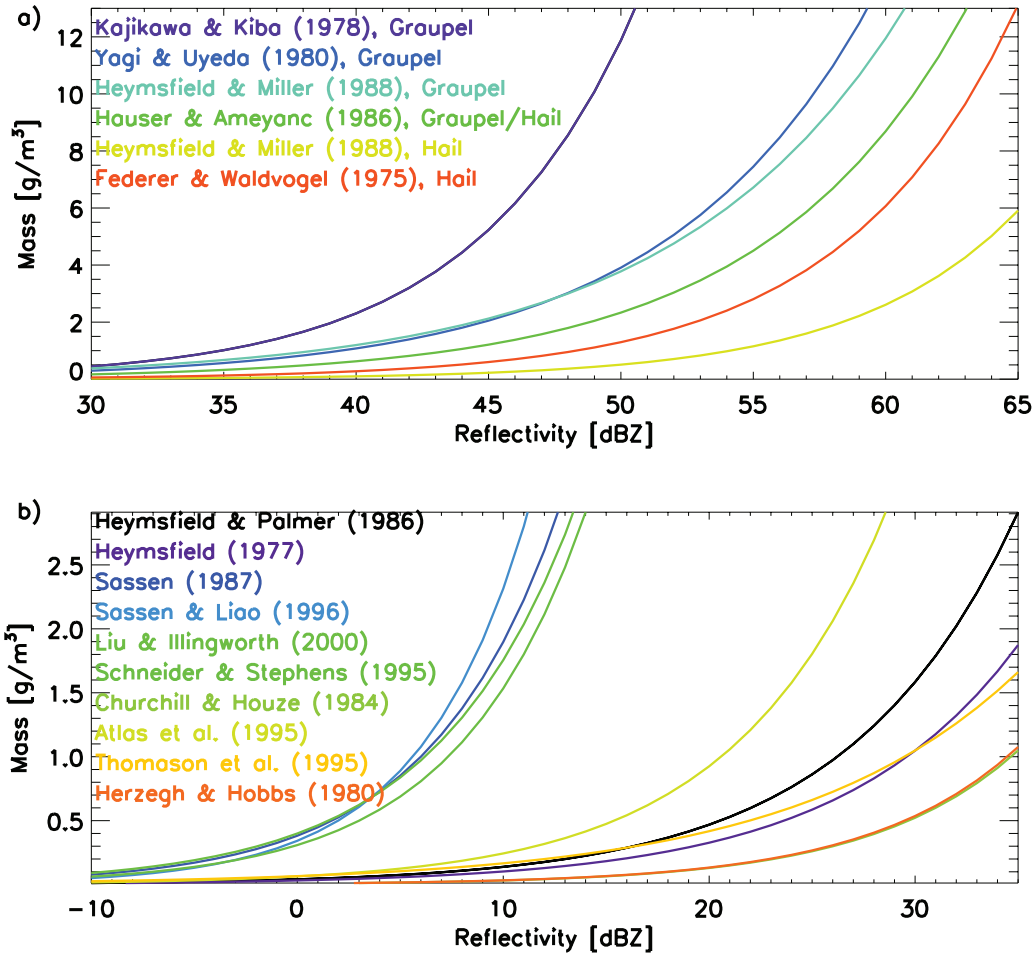

Figure 6. (a) Precipitation ice mass content (g/m^3) from different Z-M relationships of graupel and hail, respectively. (b) Nonprecipitation ice mass contents (g/m^3) from different Z-M relationships for ice crystals mass in cirrus clouds (left curves), anvil ice mass from thunderstorms (middle curves), and snow mass from stratiform portions of larger systems (right curves).

considered stable. The dry snow mass is relatively large compared to the graupel/small hail mass because of the large accumulations of ice in the thunderstorm anvil during the first stages of the 10 July storm. Note that these trends were calculated in radar space to avoid additional smoothing from gridding the data (see below). Here, individual ice mass contents were calculated for each radar gate in each Plan Positioning Indicator (PPI) scan composing a radar volume. Also the volume of the individual radar gates of each PPI scan were computed in radar space and the mass contents were then multiplied by the radar volume for each radar gate. Finally the mass values were summed over the radar volume scan. In the case of the 10 July 1996 STERAO-A, no gaps in vertical radar beams occurred but vertical beam overlaps occurred. Beam overlaps were identified and removed by applying to the lower half of an overlapping area the PID category of the lower gate and to the upper half of the overlapping area the category of the upper gate. The center time of a volume scan was assigned to the volume.

3.3.2. Influence of Different Z-M Relationships on Computed Ice Masses

[33] The sensitivity of storm total precipitation and nonprecipitation ice mass trends on different Z-M relationships was tested. Different Z-M relationships for precipitation sized ice (hail and graupel) and nonprecipitation sized ice (ice crystals mass content in cirrus clouds, anvil ice mass content from thunderstorms, snow mass content from stratiform portions of larger systems etc.) have been obtained from the literature. A collection of theoretical curves of ice mass content versus reflectivity from the literature search are presented in Figures 6a and 6b, respectively. It can be readily seen from these figures that the mass content for a particular hydrometeor category may vary up to a factor of two or more for a given reflectivity value. This is not surprising given the uncertainties in the determination of these relationships and the fact that a given radar reflectivity is produced by various combinations of particle size distributions (Z depends on D^6 and particle density).

[34] Next, different Z-M relationships for graupel, hail and nonprecipitation ice were used to calculate their storm total masses. Their time series were then compared to identify the influence of different relationships on precipitation and nonprecipitation ice mass trends. No big influences on the ice mass trends for precipitation and nonprecipitation ice were found though the actual values of the ice masses may vary by a factor of two. Correlation coefficients between ice mass

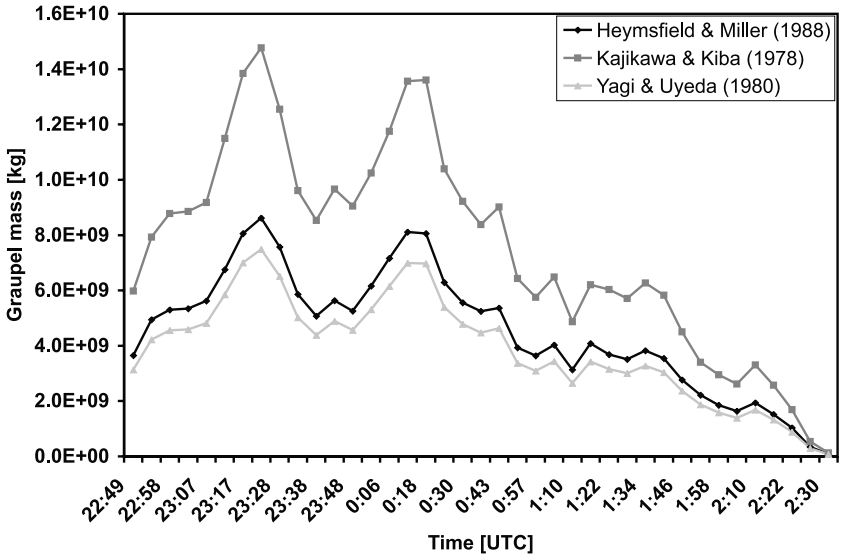

Figure 7. Time series of graupel mass above −5°C for the 10 July 1996 STERAO-A storm obtained from Z-M relationships from *Heymsfield and Miller* [1988], *Yagi and Uyeda* [1980], and *Kajikawa and Kiba* [1978], respectively. Calculations were performed in radar space. The correlation coefficients between combinations of two time series were above 0.99 in all three cases.

trends obtained from different Z-M relationships were higher than 0.99. As an example, Figure 7 shows the time series of graupel mass above −5°C obtained from three different Z-M relationships [*Heymsfield and Miller*, 1988; *Yagi and Uyeda*, 1980; *Kajikawa and Kiba*, 1978 (see also Figure 6a)] for the 10 July 1996 STERAO-A storm. Calculations were performed in radar space as described in section 3.2. Though graupel mass trends vary by a factor of two between *Yagi and Uyeda* [1980] and *Kajikawa and Kiba* [1978], the correlation coefficients between all three time series are above 0.99. From these results it was concluded that different Z-M relationships have a very minor effect on the *trends* of precipitation and nonprecipitation ice masses. Nevertheless estimated ice mass values may deviate from actual values by a factor of two. Actual ice masses are impossible to determine because we only have reflectivity values available for these calculations and no further information on particle size distributions, particle density, etc., of the sampled volumes in thunderstorms. The Z-M relationships for graupel, hail and anvil ice from *Heymsfield and Miller* [1988] and *Heymsfield and Palmer* [1986] were chosen for the analysis that follows. They were considered to represent ice mass trends sufficiently because they originate from Montana thunderstorms investigated during CCOPE.

3.3.3. Gridding Effects on Calculations of Ice Masses

[35] Finally, sensitivity tests on the influence of gridding the radar data on ice mass trends were performed. Precipitation and nonprecipitation ice mass trends were calculated in radar space and Cartesian space with different grid spacing and different radii of influence and compared. Recall that the NCAR REORDER software with a closest point gridding scheme was used to convert PID information and reflectivity from radar space into Cartesian space. Of all of the sensitivity tests performed, the largest differences in time series trends occurred between ice mass trends calculated in radar space and Cartesian space. Here the ice masses may also differ by a factor of two from radar space to Cartesian space but their time series trends have a correlation coefficient around 0.95 for both precipitation ice and nonprecipitation ice mass trends. As an example, Figure 8 shows the time series of precipitation ice mass storm totals (with *Heymsfield and Miller*'s [1988] Z-M relationships) above −5°C for the 10 July 1996 STERAO-A storm calculated in radar space and on two Cartesian grids. The first Cartesian grid has a grid spacing of 1.2 km in (x, y) and 500 m in the vertical which is consistent with the Cartesian grid of the VDRAS analysis. The radius of influence was 1.2 km for (x, y) directions and 700 m in the vertical. The second Cartesian grid had a grid spacing of 500 m in (x, y, z) directions with a radius of influence of 700 m. Precipitation ice mass trends and values from both Cartesian grids were nearly identical with a correlation coefficient of 0.999 whereas the precipitation ice mass trends between the Cartesian grids and radar space differed more with correlation coefficients of 0.96. Ice mass values differed by a factor of two or less.

[36] Differences between ice mass trends calculated in the two different coordinate systems can be caused by the closest point gridding scheme and inevitable data smoothing from the gridding procedure. Though, the trend between ice masses calculated in Cartesian space differ more from those computed in radar coordinates than the differences caused by different membership function boundaries and Z-M relationships, gridding effects on the mass trends are small and the analysis is considered stable for conversions from one coordinate system to the other.

[37] To conclude, all three influences (membership function, Z-M relationship, and gridding procedure) on the ice mass *trends* are considered relatively minor. Nevertheless actual *values* of calculated ice masses may deviate by an

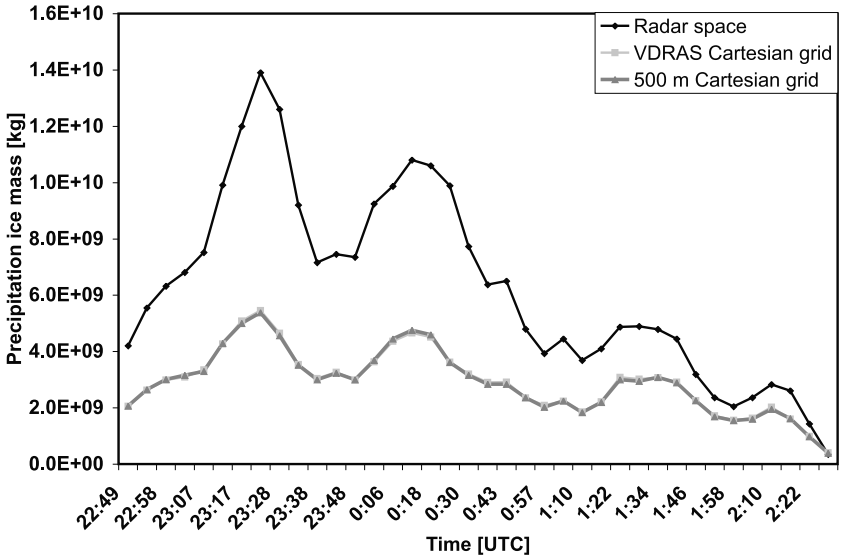

Figure 8. Time series of precipitation ice mass storm totals (with Z-M relationships from *Heymsfield and Miller* [1988]) above −5°C for the 10 July 1996 STERAO-A storm calculated in radar space and on two Cartesian grids. The first Cartesian grid (VDRAS Cartesian grid) has a grid spacing of 1.2 km in (x, y) and 500 m in the vertical which is consistent with the Cartesian grid of the VDRAS analysis. The radius of influence was 1.2 km for (x, y) directions and 700 m in the vertical. The second Cartesian grid (500-m Cartesian grid) had a grid spacing of 500 m in (x, y, z) directions with a radius of influence of 700 m.

order of magnitude, considering all three influences together on these ice masses.

4. Results

[38] In order to test the flux hypothesis, the total mass and mass fluxes of both precipitation and nonprecipitation ice within the charging zone were compared with total lightning rate on an individual storm scale for markedly different convective regimes. Six thunderstorms from the Colorado/Kansas High Plains and five from Northern Alabama were analyzed. Storm types include ordinary single cell, multicell, and supercell thunderstorms. Ice mass and ice mass flux estimates were compared to total lightning activity for all investigated thunderstorms together. For all quantified relationships between ice masses and ice mass fluxes and total lightning activity only data points that were accompanied by lightning activity were included in the analysis.

[39] It is important to note that the radar and lightning measurements have different temporal and spatial resolutions. The lightning measurements used herein have a very high spatial (a few hundred meters) and temporal (order of μs) resolution. Lightning also is a countable discrete quantity. In contrast, radar measurements have a lower spatial (a few hundred meters to kilometers) and temporal resolution (order of several minutes). Radar volume scans are composed of time integrated spatial "snapshots" from parts of thunderstorms. They give a measure of the "mean" ice mass/ice mass flux over a radar volume time (duration of four to seven minutes). To match the radar and lightning time scales the mean number of total lightning flashes per minute averaged over the radar volume time was computed. This is referred to as mean total lightning in the following.

[40] Note also, that the population of lightning flashes can be assumed to be Poisson distributed (e.g., *Petrov and D'Alessandro*, 2002; *Rakov and Uman*, 2003), as the distribution describes the probability of discrete events (flashes) that occur in a fixed time with an average (flash) rate. Hence, to express statistical variations in the lightning flash rates, the standard deviation (which is the square root of the mean for a Poisson distribution) is indicated on scatterplots showing total lightning activity as a function of ice mass or ice mass fluxes. Note, that there do not appear to be any systematic differences between ice masses or their fluxes and the lightning rate calculated from the ONERA interferometer versus the LMA measurements (not shown).

4.1. Relationship Between Flux Estimates and Product to Total Lightning Rate

[41] First, to test whether the proposed relationship $f = C{\cdot}p{\cdot}F_i$ is valid on the storm scale for a variety of storm types and environments, total storm ice mass fluxes and some of their components were compared to mean total storm lightning activity at each radar volume collection time for all 11 thunderstorms listed in Table 1. The flux hypothesis predicts a linear relationship between total lightning and ice masses as well as their fluxes. Thus quantified relationships were obtained by calculating the linear least squares fit. Some investigators have noted that nonlinear relationships are better suited for some of the mass flux components and total lightning activity. For example, on the basis of simple scaling arguments discussed by *Boccippio* [2002], the

Table 4. Exponential, Logarithmic, Power Law and for Comparison Linear Least Square Fits of Mean Total Lightning Per Minute Averaged Over the Radar Volume Time and Ice Mass Fluxes and Their Flux Components

	Exponential Function and r	Logarithmic Function and r	Power Law and r	Linear Function and r
Precipitation ice mass flux p and f	$f = 3.9e^{3.9E-10p}$, r = 0.82	$f = 32 \cdot \ln(p) - 603$, r = 0.59	$f = 5.2 \cdot 10^{-7}\, p^{0.82}$, r = 0.85	$f = 2.5 \cdot 10^{-8} p - 17.6$, r = 0.93
Nonprecipitation ice mass flux F_i and f	$f = 4.45\, e^{0.0000017\, F_i}$, r = 0.76	$f = 54.4 \cdot \ln(F_i) - 625$, r = 0.69	$f = 1.3 \cdot 10^{-5} F_i^{1.1}$, r = 0.78	$f = 1.18 \cdot 10^{-4} F_i - 14.8$, r = 0.93
Flux product pF_i and f	$f = 7.3\, e^{1.1-16(pFi)}$, r = 0.68	$f = 23.0 \cdot \ln(pF_i) - 707$, r = 0.67	$f = 2.4 \cdot 10^{-7} (pF_i)^{0.54}$, r = 0.88	$f = 9.0 \cdot 10^{-15} (F_i p) + 13.4$, r = 0.96
Precipitation ice mass p_m and f	$f = 3.92\, e^{5.3E-10(pm)}$, r = 0.82	$f = 22.7 \cdot \ln(p_m) - 608$, r = 0.59	$f = 4.9 \cdot 10^{-7} p_m^{0.84}$, r = 0.86	$f = 3.4 \cdot 10^{-8} p_m - 18.1$, r = 0.94
Nonprecipitation ice mass NPIM_T and f	$f = 5.8\, e^{5.5E-10(NPIM_T)}$, r = 0.70	$f = 30.8 \cdot \ln(NPIM_T) - 545$, r = 0.60	$f = 2.1 \cdot 10^{-5}\, NPIM_T^{0.68}$, r = 0.74	$f = 3.8 \cdot 10^{-8}\, NPIM_T + 4.0$, r = 0.85
Nonprecipitation ice mass NPIM_DIV and f	$f = 4.1\, e^{3.6E-9(NPIM_DIV)}$, r = 0.76	$f = 59.8 \ln(NPIM_DIV) - 1070$, r = 0.69	$f = 2.7 \cdot 10^{9} NPIM_DIV^{1.2}$, r = 0.76	$f = 2.5 \cdot 10^{-7}\, NPIM_DIV - 19.8$, r = 0.93

relationship between mean updraft speed above the melting level and total lightning activity can be described by a power law. Thus nonlinear least squares fits were also computed together with a value of the coefficient of determination obtained from a transformed regression model to investigate whether they are more representative of the flux hypothesis than the linear relationship. These functions include power law, exponential and a logarithmic function and are given in Table 4 for the relationships of mean total lightning and the product of the ice mass fluxes as well as some of their components. In all cases the linear fit to the data best represents their relationships.

[42] First focusing on the flux product - total lightning relationship, Figure 9 shows a scatterplot of mean total lightning versus the product of precipitation ice mass flux [$kg \cdot m \cdot s^{-1}$] and nonprecipitation ice mass flux estimate [$kg \cdot s^{-1}$] above the −5°C level with units of $kg^2 \cdot m \cdot s^{-2}$ for individual radar volumes on a logarithmic scale. The least squares fits of the data to various functions described above and their corresponding correlation coefficients were calculated (see Table 4). As predicted by *Blyth et al.* [2001], the linear fit represents best the relationship between the ice mass flux product ($C \cdot p \cdot F_i$) and total amount of lightning (f) with a correlation coefficient of 0.96. Note that the linear fits are not a straight line on the logarithmic scale plots because the intercept is not zero. In Figure 9, data are color coded so that the gray points represent data from Northern Alabama and the black points represent data from the Colorado/Kansas High Plains. The linear correlation coefficients computed for these two regions separately are also high with values of 0.99 and 0.96, respectively. The slopes of the least square fits are fairly similar to those including all data points (Table 5). This indicates that the general relationship between the product of precipitation and nonprecipitation ice mass flux and total lightning is insensitive to these different climate environments. The intercept of the fits is different which is partly caused by the limited number of data points for Northern Alabama (36 points).

[43] The product of the ice mass fluxes also correlates to the mean total lightning on a storm by storm basis. The correlation coefficient varies between 0.65 and 0.9 for individual cases and is less for ordinary single cell storms compared to severe storms. For ordinary single cell storms, small fluctuations of lightning activity (at the order of a few flashes per minute) may not necessarily be represented by the ice mass flux product. Here we may be closer to the "threshold" in the relationship of total lightning and ice mass flux product where no lightning occurs for a given ice mass flux product (similar to the argument concerning the total lightning - precipitation ice mass relationship presented by *Petersen et al.* [2005a]). Thus small fluctuations of lightning flash rate may not be seen represented by the ice mass flux product because of uncertainties in the determination of lightning flashes and ice mass/ice mass fluxes. Additionally, small fluctuations in flash rate may not be represented by the ice mass flux product because of the statistical nature of lightning flashes. As an example of a single cell storm, Figure 10 shows the product of the nonprecipitation ice mass flux and precipitation ice mass flux above the −5°C level (black solid line) and mean total lightning activity per radar volume time (gray dashed line). It can be seen that the trend of the flux product generally

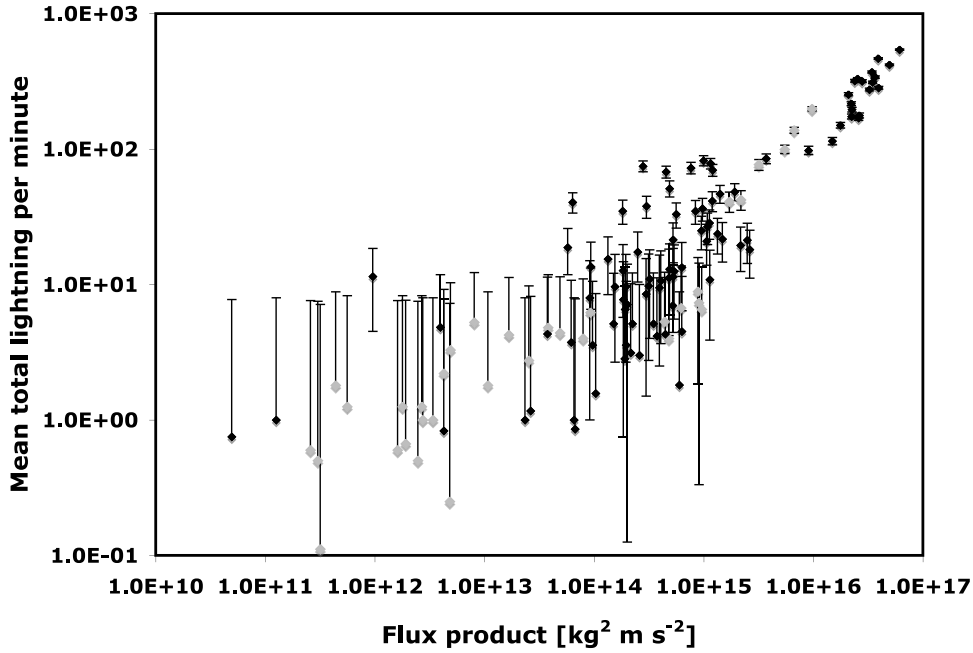

Figure 9. Mean total lightning per minute averaged over the radar volume time versus the product of nonprecipitation ice mass flux estimate and precipitation ice mass flux (kg^2 m s^{-2}) above −5°C for individual radar volumes of all 11 thunderstorms listed in Table 1. The black dots mark data from the Colorado/Kansas High Plains, whereas the gray dots mark data from Northern Alabama.

follows the trend of mean total lightning activity and the correlation coefficient is 0.67.

[44] In the following, we investigate the relationships between total lightning activity and individual ice mass components of the fluxes.

4.2. Precipitation Ice Mass and Total Lightning Rate

[45] Precipitation ice mass (p_m) above the −5°C level was calculated and compared to mean total lightning activity (from *Latham et al.* [2007, Figure 11]). A linear fit represents best the relationship between p_m and mean total lightning activity with a correlation coefficient of 0.94. The linear functions of the fits for storms from all data and data partitioned for storms occurring only in Northern Alabama and only in the High Plains regions are listed in Table 6 (see Table 4 for the functions of the other fits). Remarkably, the empirically derived functions for storms in Northern Alabama and the High Plains are similar, even considering uncertainties in the determination of precipitation ice and total lightning activity mentioned in section 3.

[46] Figure 11 implies that precipitation ice is related to total lightning in a close to linear fashion for different types of thunderstorms in different environments on a storm scale. These results compliment the findings of *Petersen and Rutledge* [2001], *Petersen et al.* [2005a], and *Latham et al.* [2007] who presented observational evidence for an essentially linear relationship between precipitation ice mass and total lightning for different climate regimes on a global scale.

[47] To further refine the relationship between lightning and precipitation ice mass, the precipitation ice mass was separated into graupel mass and hail categories by combining the NCAR PID categories of Graupel/Small hail together with Graupel/Small hail/Rain and combining Hail together with Hail/Rain. The radar signal from the latter categories is likely dominated by hail with diameters greater than 5 mm [*Straka et al.*, 2000] in the presence of graupel. Nevertheless, polarimetric signatures between high-density graupel and small to medium sized hail are similar and have considerable overlap. Only focusing on the reflectivity membership function for example, the Graupel/Small hail and Hail categories overlap between 48 dBZ and 55 dBZ herein similar to what is suggested by *Straka et al.* [2000] or *Doviak and Zrnic* [1993].

[48] Figure 12a shows a scatterplot of graupel mass (p_{gm}) above the −5°C level and mean total lightning from

Table 5. Expressions for the Linear Fits of Mean Total Lightning Per Minute Averaged Over the Radar Volume Time and the Product of Precipitation and Nonprecipitation Ice Mass Fluxes ($kg^2 \cdot m \cdot s^{-2}$) Above the −5°C Level

	All Data Points	Data Points from Northern Alabama	Data points from the Colorado/Kansas High Plains
Linear function	$f = 9.0 \cdot 10^{-15}$ ($F_i p$) + 13.4	$f = 2 \cdot 10^{-14} F_i \cdot p + 2.7$	$f = 8.8 \cdot 10^{-15}$ ($F_i p$) + 15.3
Correlation coefficient r	0.96	0.99	0.96

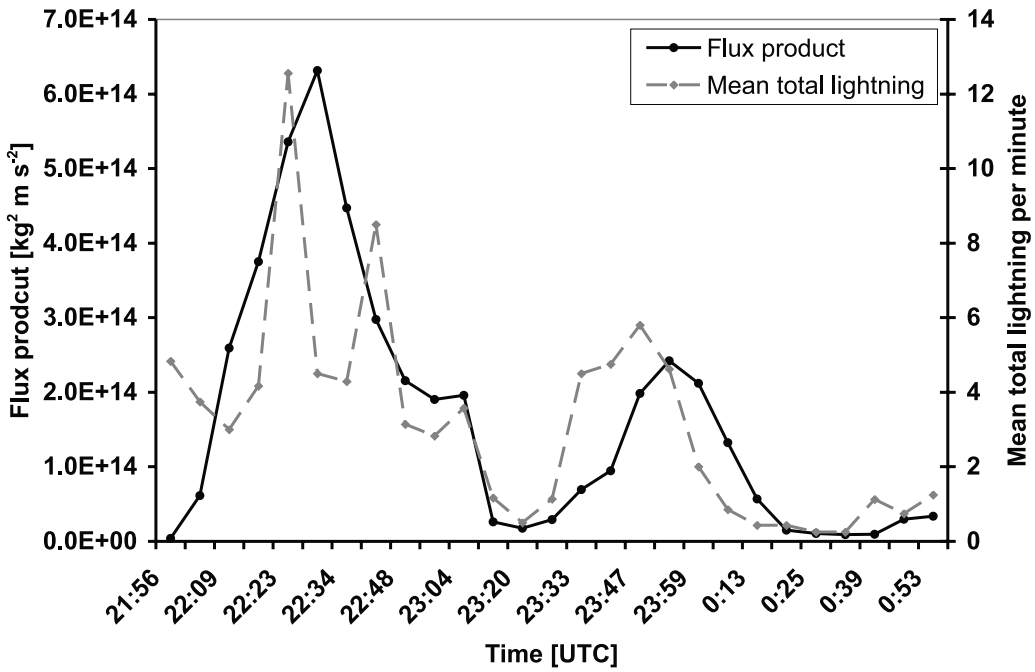

Figure 10. Mean total lightning rate per minute averaged over the radar volume time (gray dashed line) and the product of the fluxes of precipitation ice mass above the −5°C level and nonprecipitation ice mass above the −5°C level calculated with the divergence method (black solid line) of an ordinary single cell thunderstorm that occurred on 6 June 2000.

individual radar volumes for all investigated thunderstorms on a logarithmic scale. The graupel mass was computed with the Z-M relationship from *Heymsfield and Miller* [1988] listed in Table 2. In Figure 12a, data points are only included if they contained graupel and lightning activity. The relationship between the graupel mass and mean total lightning from individual radar volumes is close to linear with a correlation coefficient of 0.94. Once again, the linear fit best represented the mass-lightning relationship, similar to the total precipitation ice mass-mean total lightning relationship. A power law fit was the second best fit to the data with r = 0.86. Here f was proportional to $p_{gm}^{0.83}$ which also suggests a close to linear relationship. The functions and coefficients for the fits are given in Table 7.

[49] Figure 12b shows a scatterplot of hail mass (p_{hm}) above the −5°C level and mean total lightning from individual radar volumes for all investigated thunderstorms on a logarithmic scale. The hail mass was computed with the Z-M relationship from *Heymsfield and Miller* [1988] also listed in Table 2. The relationship between hail mass and total lightning activity with a linear correlation coefficient of 0.72 is not as strong as graupel mass and total lightning activity. This is in agreement with results of the 29 June 2000 STEPS supercell storm from *Wiens et al.* [2005]. Linear and power law fits represent the relationship between hail mass and mean amount of total lightning best and equations of the fits together with coefficients are given in Table 7.

[50] This suggests that riming graupel pellets play a more dominant role than hail in thunderstorm electrification. One reason may be that the number concentration of the largest hailstones that dominate the radar signal is low. Thus the integrated hail surface area that can undergo collisions with ice crystals is much smaller compared to the integrated surface area from a much higher number concentration of graupel pellets [*Williams*, 2001]. Consequently, hailstones may not contribute as much to electrification. Another reason may be that hailstones undergoing wet growth accompanied by high LWC in severe storms may not separate charge in collisions with ice crystals [*Saunders and Brooks*, 1992].

[51] Note that the hail mass is more than an order of magnitude less than the graupel mass, i.e., graupel dominates the precipitation ice mass calculations.

4.3. Nonprecipitation Ice Mass Estimates and Total Lightning

[52] Two estimates of nonprecipitation ice mass from the charging zone were computed and compared to total lightning activity. As a first estimate, nonprecipitation ice mass above the −50°C level with reflectivity values

Table 6. Linear Fit of Mean Total Lightning Per Minute Averaged Over the Radar Volume Time and Precipitation Ice Mass (kg) Above the −5°C Level

	All Data Points	Data Points from Northern Alabama	Data Points from the Colorado/Kansas High Plains
Linear function	$f = 3.4 \cdot 10^{-8} p_m - 18.1$	$f = 2.73 \cdot 10^{-8} p_m - 5.1$	$f = 3.5 \cdot 10^{-8} p_m - 23.4$
Correlation coefficient r	0.94	0.93	0.94

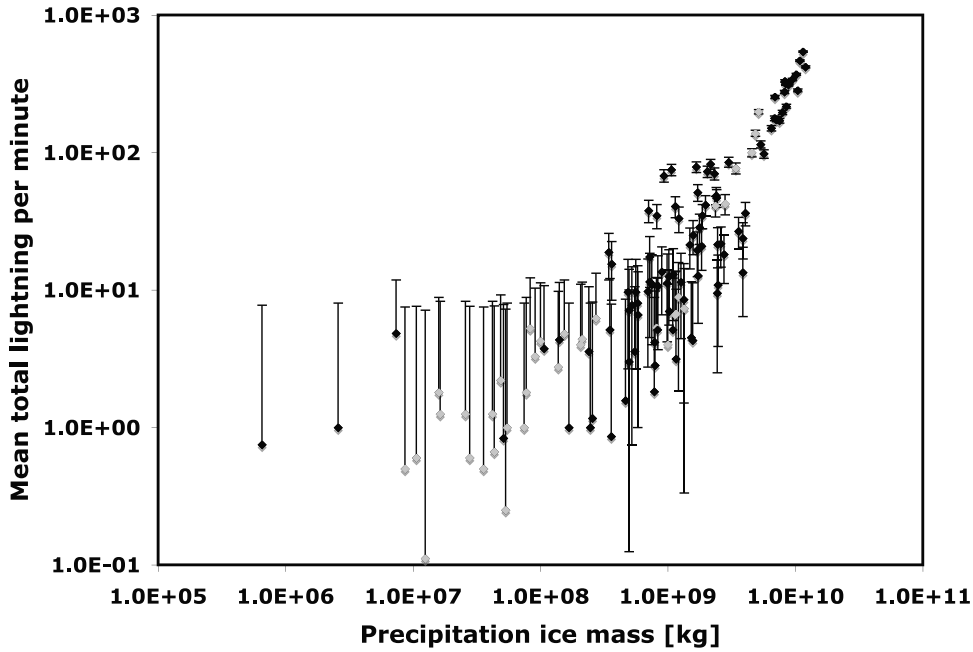

Figure 11. Mean total lightning per minute averaged over the radar volume time versus precipitation ice mass (kg) above the −5°C level for individual radar volumes of all 11 thunderstorms [from *Latham et al.*, 2007]. The black dots mark data from the Colorado/Kansas High Plains, whereas the gray dots mark data from Northern Alabama.

below 20 dBZ (NPIM_T) was calculated as described in section 3.2. Figure 13a shows the scatterplot of NPIM_T and mean total lightning on a logarithmic scale. A linear function given in Table 8, gives the best least squares fit to the data with a linear correlation coefficient of 0.85 (Table 4 shows the other least squares fits). Linear fits for data from Northern Alabama and the Colorado/Kansas High Plains, respectively, differ from the fit for all data points but also have high correlation coefficients of 0.89 and 0.86, respectively. This suggests that a relationship exists between nonprecipitation ice and total lightning, even though this is a very rough estimate for nonprecipitation ice mass from the charging zone. This result is in some agreement with results from *Sherwood et al.* [2006]. They compared seasonal total lightning counts from LIS and OTD (flashes per square km per months) averaged over the years 1999–2003 and the seasonal ice particle effective diameter (mean volume divided by the mean surface area of particles) derived from brightness temperatures over the years 1984 to 1998. They conclude that their results show a relationship between total lightning counts and amounts of small ice (with effective diameters smaller than 30 μm) at cloud top

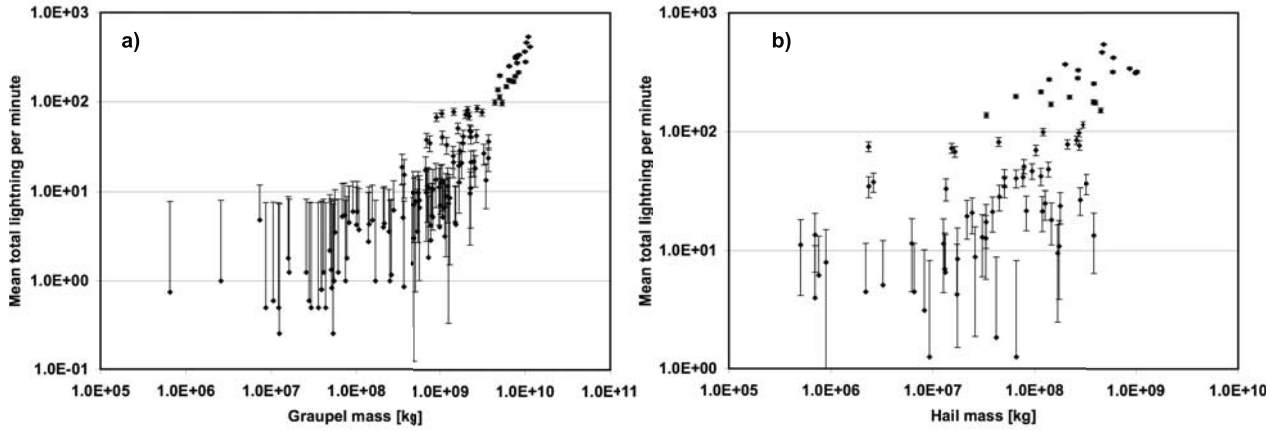

Figure 12. (a) Mean total lightning per minute averaged over the radar volume time versus graupel mass (kg) above the −5°C level for individual radar volumes of all 11 thunderstorms. (b) Mean total lightning per minute averaged over the radar volume time versus hail mass (kg) above the −5°C level for individual radar volumes of all 11 thunderstorms.

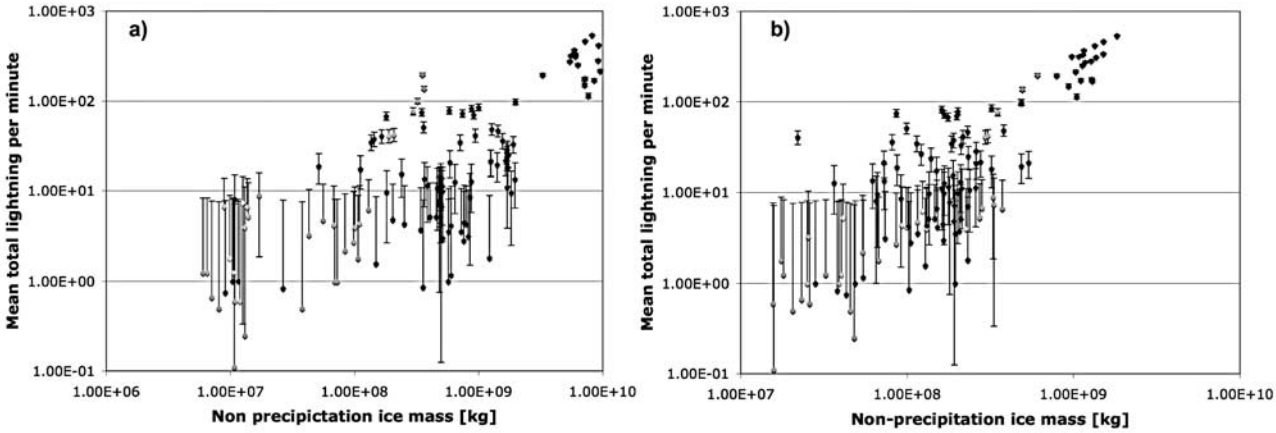

Figure 13. (a) Mean total lightning per minute averaged over the radar volume time versus NPIM_T (kg) for individual radar volumes of all 11 thunderstorms listed. The black dots mark data from the Colorado/Kansas High Plains, whereas the gray dots mark data from Northern Alabama. (b) Mean total lightning per minute averaged over the radar volume time versus NPIM_DIV (kg) above the −5°C level for individual radar volumes of all 11 thunderstorms [from *Latham et al.*, 2007]. The black dots mark data from the Colorado/Kansas High Plains, whereas the gray dots mark data from Northern Alabama.

which is in agreement with the above result. Nevertheless they found no evidence that total lightning is related to the volume or cloud ice mass at lower altitudes though they acknowledge that the cloud ice at the top of the cloud may be related to that in lower altitudes.

[53] As described in section 3.2, nonprecipitation ice above a temperature threshold and coincident with divergence values larger than 0.001 s^{-1} and reflectivity values below 20 dBZ were chosen as a second estimate to represent nonprecipitation ice from the charging zone. Figure 13b shows this nonprecipitation ice mass estimate above the −5°C level versus mean total lightning on a logarithmic scale [*Latham et al.*, 2007]. This estimate will be referred to as NPIM_DIV in the following. Similar to the NPIM_T, the relationship between NPIM_DIV and mean total lightning is represented best with a linear fit. The correlation of NPIM_DIV and total lightning activity is higher with a correlation coefficient of 0.93 than the one involving NPIM_T (r = 0.85). This suggests a strong linear relationship between nonprecipitation ice mass and total lightning [*Latham et al.*, 2007]. The function of the linear fit between NPIM_DIV and mean total lightning is presented in Table 9 together with linear fit relationships for the individual data from the two regions. All linear fits are nearly identical. The trends of NPIM_DIV do not change very much by varying the temperature threshold from −5°C to lower temperatures of −35°C or −40°C (representative of the upper part of the charging zone), though values of NPIM_DIV above −35°C or −40°C compared to −5°C can be less for smaller ordinary single cell thunderstorms because the thunderstorm height is lower than for stronger thunderstorms. However, the correlation coefficient between NPIM_DIV and mean total lightning remains at 0.93 with similar linear relationships among the different thresholds. For example, the linear fit for all data points between mean nonprecipitation ice mass above −40°C is $f = 2.85 \cdot 10^{-7} NPIM_DIV + 0.93$. Nonprecipitation ice mass above the −5°C level was chosen for the NPIM_DIV over colder temperature thresholds for the following reasons:

[54] • Smaller ice particles in the updraft (and in the charging zone above the melting level) are carried not only upward but also laterally outward into the anvils of thunderstorms [e.g., *Yuter and Houze*, 1995]. Thus threshold temperatures colder than −5°C may lead to underestimation of nonprecipitation ice mass.

[55] • Colder temperature thresholds may not capture all smaller ice particles exiting the charging zone as weakly electrified ordinary thunderstorms may not exhibit storm tops colder than temperatures of −40°C.

[56] • Multicellular thunderstorms may have updraft areas at various heights. Some of these updraft areas may not exceed temperatures of −40°C again leading to underestimates of nonprecipitation ice mass.

5. Summary and Discussion

[57] The main goals of this study were to examine observational evidence on a storm scale for a variety of

Table 7. Linear Fit Relationships and Power Law Fits for Mean Total Lightning Per Minute Averaged Over the Radar Volume Time and Hail and Graupel Mass (kg) Above the −5°C Level, Respectively[a]

	Hail Mass-Mean Total Lightning	Graupel Mass-Mean Total Lightning
Linear function	$F = 4.1 \cdot 10^{-7} p_{hm} + 28.1$	$f = 3.6 \cdot 10^{-8} p_{gm} - 16.2$
Correlation coefficient r	0.72	0.94
Power law	$F = 0.0035 p_{hm}^{0.52}$	$f = 6.4 \cdot 10^{-7} p_{gm}^{0.83}$
Correlation coefficient r	0.65	0.86

[a]The fits were only performed for data points that had hail and graupel mass as well as lightning activity.

Table 8. Linear Fit of Mean Total Lightning Per Minute Averaged Over the Radar Volume Time and NPIM_T (kg)

	All Data Points	Data Points from Northern Alabama	Data Points from the Colorado/Kansas High Plains
Linear function	$f = 3.8 \cdot 10^{-8}$ NPIM_T + 4.0	$f = 3.7 \cdot 10^{-7}$ NPIM_T-10.5	$f = 3.9 \cdot 10^{-8}$NPIM_T-2.7
Correlation coefficient r	r = 0.85	0.89	0.86

storm types and environments in order to test the validity of the flux hypothesis and to quantify the relationship $f = C \cdot p \cdot F_i$. Additional goals were to investigate the relationship between precipitation ice mass content and total lightning activity on a storm scale, in order to refine the global observations of *Petersen et al.* [2005a].

[58] Ground-based dual-Doppler and polarimetric radar data were used to derive precipitation and nonprecipitation ice mass fluxes together with total lightning information from ground-based total lightning networks to observationally evaluate the validity of the flux hypothesis. Data from 11 storms of different types, including ordinary single cell, multicell, and supercell thunderstorms, from the Colorado/Kansas High Plains and Northern Alabama were examined. The results can be summarized as follows:

[59] ● For all 11 storms the product of storm total precipitation and nonprecipitation ice mass flux is well correlated to total lightning activity. This is also true on a storm by storm basis.

[60] ● The quantified relationship between the product of the ice mass fluxes F_i and p and mean total lightning rate per minute averaged over the radar volume time f for all data from the 11 storms investigated has the form

$$f = 9.0 \cdot 10^{-15} F_i \cdot p + 13.4,$$

with a correlation coefficient of 0.96.

[61] ● The relationship appears invariant between the two storm environments (High Plains and Northern Alabama). Since variations of storm type are included in the sample, we speculate that the relationship may also be relatively insensitive to the storm type.

[62] ● Precipitation and nonprecipitation ice mass flux estimates taken individually also correlate well with mean total lightning rate with correlation coefficients of 0.93 for both.

[63] ● On the storm scale, precipitation ice mass by itself is well correlated to mean total lightning rate in an approximately linear fashion for different types of thunderstorms in different environments on a storm scale (r = 0.94). This is in agreement with observations from *Petersen and Rutledge* [2001], *Petersen et al.* [2005a], and *Latham et al.* [2007] who presented observational evidence for an essentially linear relationship between precipitation ice mass and total lightning rate for different climate regimes on a global scale.

[64] ● Graupel/small hail ice mass correlates much better with mean total lightning rate than large hail ice mass.

[65] ● Nonprecipitation ice mass (NPIM_T) in the upper part of thunderclouds (above the −50°C level) is fairly well correlated to the mean total lightning rate (r = 0.85).

[66] ● Nonprecipitation ice mass (NPIM_DIV) calculated with the divergence method is well correlated with mean total lightning rate (r = 0.93) and seems to be a better estimator of nonprecipitation ice passing through the charging zone.

[67] ● The best functional representation between total lightning rate and all of the parameters tested (ice mass flux product and individual flux product components) were found to be linear. This was true for all storm types in both geographic regions.

[68] The observations as summarized provide strong observational support for the flux hypothesis presented by *Blyth et al.* [2001], verifying, to a first order, a linear relationship between the product of ice mass fluxes and total lightning rate. Furthermore, this relationship appears *robust* and *relatively invariant* for storms from the two different climate regions and of different type. This is also true for the relationship between total lightning rate and flux components such as precipitation ice mass, nonprecipitation ice mass estimates and updraft volume above the melting level. These results are in agreement with *Wiens et al.* [2005] and *Kuhlman et al.* [2006] who found good correlations between the total flash rate and graupel volume, updraft volume and updraft mass flux for the 29 June STEPS storm. Note, that the relationship between updraft strength and total lightning was investigated by *Deierling and Petersen* [2008]. Results show that there is a strong correlation between total lightning rate and updraft volume, in particular with vertical velocities above 5–10 m/s. On the basis of noninductive charging theory, this supports the idea that larger updraft volumes produce more hydrometeors in the charging zone thus leading to a higher number of collisions between graupel pellets and ice crystals and subsequent macroscale charge separation (e.g., enhanced ice fluxes) which can result in an increased lightning activity. Observations made herein also support the scaling arguments summarized by *Boccippio* [2002] that suggest that the electrical power generated is linearly related to lightning activity and should also be linearly related to the generator current density (product of net charge transport velocity and charge density). Furthermore, differences in the empirical relationships diagnosed for storms from different climate environments are small and can likely be explained by the uncertainties of mass flux calculations from radar data, limited number of data points

Table 9. Linear Fit Relationship of Mean Total Lightning Per Minute Averaged Over the Radar Volume Time and NPIM_DIV (kg) Above the −5°C Level

	All Data Points	Data Points from Northern Alabama	Data Points from the Colorado/Kansas High Plains
Linear function	$f = 2.5 \cdot 10^{-7}$ NPIM_DIV-19.8	$f = 2.1 \cdot 10^{-7}$ NPIM_DIV-14.1	$f = 2.5 \cdot 10^{-7}$ NPIM_DIV-20.5
Correlation coefficient r	r = 0.93	0.8	0.93

and the determination of total lightning activity described in section 3. The higher scatter of the ice mass flux product observed at low flash rates may not only be caused by the measurement and ice flux calculation uncertainties but also by physical reasons. At low flash rates the relationship between ice mass and ice mass fluxes and total lightning rate may compete with other charge dissipation mechanisms (e.g., conduction and precipitation currents [*Boccippio*, 2002] that contribute to the Maxwell currents) that diminish total lightning activity.

[69] Concerning the relationship between total lightning and precipitation ice mass above the melting level, results confirm a strong and relatively robust linear relationship between the two that appears invariant from the climate regime, as observed by *Petersen et al.* [2005a]. This is true down to the individual storm scale. Results presented herein (in particular the relationship between ice mass fluxes and total lightning) support strongly the prediction by *Petersen et al.* [2005a] that with "sufficient vertical fluxes of ice and associated charge generation via the noninductive-based charging mechanisms. . ..the relationship between ice water path and lightning flash density should exhibit high correlation and be independent of regime."

[70] Nonprecipitation ice mass estimates - in particular those retrieved with the divergence method, correlate very well with total lightning activity, suggesting that one may be able to use total lightning to determine ice mass that is transported into thunderstorm anvils. It should be kept in mind that the updraft area information is implicitly in the nonprecipitation ice mass estimate. Nevertheless, the equation of total lightning and nonprecipitation ice mass estimate using the divergence method predicts that $8.3 \cdot 10^7$ kg of nonprecipitation ice are associated with one lightning flash. Assuming a global flash rate of about 40 flashes per second (determined from OTD and LIS observations, *Blyth et al.* [2001]) yields a global nonprecipitation ice mass production of $3.3 \cdot 10^9$ kg/s. This is about two orders of magnitude larger than predicted by the crude estimates made by *Blyth et al.* [2001]. It should be kept in mind that the estimates of ice masses derived from radar data herein can differ by an order of magnitude as explained in section 3.

[71] Note, that scatter and reduced correlation between total lightning and ice masses as well as their fluxes are introduced by effects such as uncertainties in the measurements and in the ice mass/flux computations. The flux hypothesis assumes a steady state situation where the charge neutralized by a lightning flash is "refilled" by the ice mass fluxes. Thus an additional source of scatter is that lightning flash rates may not be representative of the amount of charge that is equalized by them. Flash frequency that is weighted by the flash lengths or the power emitted by flashes may be more representative of the amount of charge equalized by a flash and should be looked at in future research.

6. Outlook

[72] The strong correlations between precipitation and nonprecipitation ice masses, and their fluxes with total lightning rate suggest that total lightning information may be useful as a tool for estimating both ice masses and ice mass fluxes. A next step would be to investigate whether total lightning rate can be used in climate models to help estimate the nonprecipitation ice mass produced by thunderstorms, which may be of potential use in studying the radiation budget of the earth-atmosphere system [*Sherwood et al.*, 2006] or upper tropospheric water vapor [*Price and Asfur*, 2006]. For severe convection the results herein were particularly robust (not shown). This suggests that total lightning information could be useful in estimating ice mass and ice mass fluxes on a storm by storm basis for severe storms. The next step would be to expand the validation of this approach on more numerous storm data sets. If the relationships remain as robust as suggested herein, their application in thunderstorm nowcasting systems could be implemented. This may be particularly useful in regions where radar data are not available (e.g., in mountainous terrain where radar data are limited by beam blockage).

[73] Furthermore, recent work by *Mansell et al.* [2007] has shown that data assimilation of total lightning data improves the forecast of storm morphology and prediction of rainfall amounts. It would be interesting to investigate whether total lightning rate measurements in concert with the ice mass flux relationship may be useful for data assimilation with cloud scale models. Alternatively it would also be interesting to see whether one can use the ice mass flux relationship to predict total lightning, for example to estimate NO_x production in thunderstorms.

[74] **Acknowledgments.** We gratefully acknowledge the assistance and support of Jim Dye during the course of this work. We would also like to acknowledge Christelle Barthe for providing the WRF result of the STERAO-A 10 July storm, and Andrew Crook, Eric Defer, and Pat Kennedy for providing data sets and/or support in the data analysis. We also wish to acknowledge the sponsors funding this research including the NASA Earth Observing Systems and Earth Systems Sciences Programs (TRMM-LIS (John Latham); UAH-NASA Cooperative Agreement contract NNM05AA22A), the NOAA GOES-R Global Lightning Mapper Risk Reduction Project (Walter Petersen), and the National Science Foundation Advanced Studies Program (Wiebke Deierling).

References

Atlas, D., S. Y. Matrosov, A. J. Heymsfield, M.-D. Chou, and D. B. Wolff (1995), Radar and radiation properties of ice clouds, *J. Appl. Meteorol.*, *34*(11), 2329–2345.

Baker, M. B., H. J. Christian, and J. Latham (1995), A computational study of the relationships linking lightning frequency and other thundercloud parameters, *Q. J. R. Meteorol. Soc.*, *121*(527), 1525–1548.

Baker, M. B., A. M. Blyth, H. J. Christian, A. M. Gadian, J. Latham, and K. K. Miller (1999), Relationships between lightning activity and various thundercloud parameters: Satellite and modelling studies, *Atmos. Res.*, *51*(3–4), 221–236.

Barth, M. C., et al. (2007), Cloud-scale model intercomparison of chemical constituent transport in deep convection, *Atmos. Chem. Phys.*, *7*(18), 4709–4731.

Blyth, A. M., H. J. Christian, K. Driscoll, A. M. Gadian, and J. Latham (2001), Determination of ice precipitation rates and thunderstorm anvil ice contents from satellite observations of lightning, *Atmos. Res.*, *59–60*, 217–229.

Boccippio, D. J. (2002), Lightning scaling relations revisited, *J. Atmos. Sci.*, *59*(6), 1086–1104.

Bringi, V. N., G.-J. Huang, V. Chandrasekar, and T. D. Keenan (2001), An areal rainfall estimator using differential propagation phase: Evaluation using a C-band radar and a dense gauge network in the tropics, *J. Atmos. Oceanic Technol.*, *18*(5), 1810–1818.

Brunkow, D., V. N. Bringi, P. C. Kennedy, S. A. Rutledge, V. Chandrasekar, E. A. Mueller, and R. K. Bowie (2000), A description of the CSU-CHILL national radar facility, *J. Atmos. Oceanic Technol.*, *17*(12), 1596–1608.

Carey, L. D., and S. A. Rutledge (1996), A multiparameter radar case study of the microphysical and kinematic evolution of a lightning producing storm, *J. Meteorol. Atmos. Phys.*, *59*, 33–64.

Christian, H. J., et al. (1999), The Lightning Imaging Sensor, in *11th International Conference in Atmospheric Electricity*, Guntersville, AL, 7–11 June, pp. 746–749.

Churchill, D. D., and R. A. Houze Jr. (1984), Mesoscale updraft magnitude and cloud-ice content deduced from the ice budget of the stratiform region of a tropical cloud cluster, *J. Atmos. Sci.*, *41*(10), 1717–1725.

Crook, N. A., and J. Sun (2004), Analysis and forecasting of the low-level wind during the Sydney 2000 forecast demonstration project, *Weather Forecast.*, *19*(1), 151–167.

Defer, E., P. Blanchet, C. Thery, P. Laroche, J. E. Dye, M. Venticinque, and K. L. Cummins (2001), Lightning activity for the 10 July, 1996, storm during the stratosphere-troposphere experiment: Radiation, aerosol, and ozone-A (STERAO-A) experiment, *J. Geophys. Res.*, *106*(D10), 10,151–10,172.

Deierling, W. (2006), The relationship between total lightning and ice fluxes, Ph.D. dissertation, Univ. of Alabama in Huntsville, Huntsville, Ala., 175 pp.

Deierling, E., and W. A. Petersen (2008), Total lightning activity as an indicator or updraft characteristics, *J. Geophys. Res.*, doi:10.1029/2007JD009598, in press.

Deierling, W., W. A. Petersen, J. Latham, S. M. Ellis, and H. J. Christian Jr. (2005), On the relationship of thunderstorm ice hydrometeor characteristics and total lightning measurements, *Atmos. Res.*, *76*(1–4), 114–126.

Doviak, R. J., and D. S. Zrnic (1993), *Doppler Radar and Weather Observations*, 562 pp., Academic Press, San Diego, CA.

Dye, J. E., J. J. Jones, A. J. Weinheimer, and W. P. Winn (1989), Observations within two regions of charge during initial thunderstorm electrification, *Q. J. R. Meteorol. Soc.*, *114*(483), 1271–1290.

Dye, J. E., et al. (2000), An overview of the Stratospheric-Tropospheric Experiment: Radiation, Aerosols, and Ozone (STERAO)-Deep Convection experiment with results for the July 10, 1996 storm, *J. Geophys. Res.*, *105*(D8), 10,023–10,046.

Federer, B., and A. Waldvogel (1975), Hail and raindrop size distributions from a Swiss multicell storm, *J. Appl. Meteorol.*, *14*(1), 91–97.

Ferrier, B. S. (1994), A double-moment multiple-phase four-class bulk ice scheme. part I: Description, *J. Atmos. Sci.*, *51*(2), 249–280.

Goodman, S. J., et al. (2005), The North Alabama Lightning Mapping Array: Recent severe storm observations and future prospects, *Atmos. Res.*, *76*(1–4), 423–437.

Hauser, D., and P. Amayenc (1986), Retrieval of cloud water and water vapor contents from Doppler radar data in a tropical squall line, *J. Atmos. Sci.*, *43*(8), 823–838.

Herzegh, P. H., and P. V. Hobbs (1980), The mesoscale and microscale structure and organization of clouds and precipitation in midlatitude cyclones. II: Warm-frontal clouds, *J. Atmos. Sci.*, *37*(3), 597–611.

Heymsfield, A. J. (1977), Precipitation development in stratiform ice clouds: A microphysical and dynamical study, *J. Atmos. Sci.*, *34*(2), 367–381.

Heymsfield, A. J., and A. G. Palmer (1986), Relations for deriving thunderstorm anvil mass of CCOPE storm water budget estimates, *J. Clim. Appl. Meteorol.*, *25*(5), 691–702.

Heymsfield, A. J., and K. M. Miller (1988), Water vapor and ice mass transported into the anvils of CCOPE thunderstorms: Comparison with storm influx and rainout, *J. Atmos. Sci.*, *45*(22), 3501–3514.

Jayaratne, E. R., C. P. R. Saunders, and J. Hallett (1983), Laboratory studies of the charging of soft hail during ice crystal interactions, *Q. J. R. Meteorol. Soc.*, *109*(461), 609–630.

Kajikawa, M., and K. Kiba (1978), Observation of the size distribution of graupel particles, *Tenki*, *25*, 390–398.

Keith, W. D., and C. P. R. Saunders (1990), Further laboratory studies of the charging of graupel during ice crystal interactions, *Atmos. Res.*, *25*(5), 445–464.

Kuhlman, K. M., C. L. Ziegler, E. R. Mansell, D. R. MacGorman, and J. M. Straka (2006), Numerically simulated electrification and lightning of the 29 June 2000 STEPS supercell storm, *Mon. Weather Rev.*, *134*(10), 2734–2757.

Lang, T. J., et al. (2004), The severe thunderstorm electrification and precipitation study, *Bull. Am. Meteorol. Soc.*, *85*(8), 1107–1125.

Laroche, P., A. Bondiou, P. Blanchet, and J. Pigere (1994), 3D VHF mapping of lightning discharge within a storm, paper presented at Foudre et montage 94, Chamonix, France.

Latham, J., A. M. Blyth, H. J. Christian Jr., W. Deierling, and A. M. Gadian (2004), Determination of precipitation rates and yields from lightning measurements, *J. Hydrol.*, *288*(1–2), 13–19.

Latham, J., W. A. Petersen, W. Deierling, and H. J. Christian (2007), Field identification of a unique globally dominant mechanism of thunderstorm electrification, *Q. J. R. Meteorol. Soc.*, *133*, 1453–1457, doi:10.1002/qj.133.

Lin, Y.-L., R. D. Farley, and H. D. Orville (1983), Bulk parameterization of the snow field in a cloud model, *J. Appl. Meteorol.*, *22*(6), 1065–1092.

Liu, C.-L., and A. J. Illingworth (2000), Toward more accurate retrievals of ice water content from radar measurements of clouds, *J. Appl. Meteorol.*, *39*(7), 1130–1146.

Liu, H., and V. Chandrasekar (2000), Classification of hydrometeors based on polarimetric radar measurements: Development of fuzzy logic and neuro-fuzzy systems, and in situ verification, *J. Atmos. Oceanic Technol.*, *17*(2), 140–164.

MacGorman, D. R., W. D. Rust, P. Krehbiel, W. Rison, E. Bruning, and K. Wiens (2005), The electrical structure of two supercell storms during STEPS, *Mon. Wea. Rev.*, *133*(9), 2583–2607.

Mansell, E. R., D. R. MacGorman, C. L. Ziegler, and J. M. Straka (2005), Charge structure and lightning sensitivity in a simulated multicell thunderstorm, *J. Geophys. Res.*, *110*, D12101, doi:10.1029/2004JD005287.

Mansell, E. R., C. L. Ziegler, and D. R. MacGorman (2007), A lightning data assimilation technique for mesoscale forecast models, *Mon. Weather Rev.*, *135*(5), 1732–1748.

Marks, F. D., Jr., and R. A. Houze Jr. (1987), Inner core structure of hurricane Alicia from airborne Doppler radar observations, *J. Atmos. Sci.*, *44*(9), 1296–1317.

Mohr, C. G., L. J. Miller, R. L. Vaughn, and H. W. Frank (1986), On the merger of mesoscale datasets into a common Cartesian format for efficient and systematic analysis, *J. Atmos. Oceanic. Technol.*, *3*(1), 143–161.

Nesbitt, S. W., E. J. Zipser, and D. J. Cecil (2000), A census of precipitation features in the tropics using TRMM: Radar, ice scattering and lightning observations, *J. Clim.*, *13*(23), 4087–4106.

Pereyra, R. G., E. E. Avila, N. E. Castellano, and C. Saunders (2000), A laboratory study of graupel charging, *J. Geophys. Res.*, *105*(D16), 20,803–20,812.

Petersen, W. A., and S. A. Rutledge (2001), Regional variability in tropical convection: Observations from TRMM, *J. Clim.*, *14*(17), 3566–3586.

Petersen, W. A., S. A. Rutledge, and R. E. Orville (1996), Cloud-to-ground lightning observations to TOGA COARE: Selected results and lightning location algorithm, *Mon. Weather Rev.*, *124*(4), 602–620.

Petersen, W. A., S. A. Rutledge, R. C. Cifelli, B. S. Ferrier, and B. F. Smull (1999), Shipborne Dual-Doppler operations during TOGA COARE: Integrated observations of storm kinematics and electrification, *Bull. Am. Meteorol. Soc.*, *80*(1), 81–96.

Petersen, W. A., H. J. Christian, and S. A. Rutledge (2005a), TRMM observations of the global relationship between ice water content and lightning, *Geophys. Res. Lett.*, *32*, L14819, doi:10.1029/2005GL023236.

Petersen, W. A., et al. (2005b), The UAH-NSSTC/WHNT ARMOR C-band dual-polarimetric radar: A unique collaboration in research, education and technology transfer, in *Preprints of the 32nd AMS Radar Meteorology Conference*, *Albuquerque*, NM, 24–29 October, CD-ROM, AMS.

Petrov, N. I., and F. D'Alessandro (2002), Verification of lightning strike incidence as a Poisson process, *J. Atmos. Terr. Phys.*, *64*(15), 1645–1650.

Price, C., and M. Asfur (2006), Can lightning observations be used as an indicator of upper-tropospheric water vapor variability?, *Bull. Am. Meteorol. Soc.*, *87*(3), 291–298.

Pruppacher, H. R., and J. D. Klett (1997), *Microphysics of Clouds and Precipitation*, pp. 954, Kluwer Acad., Dordrecht, Netherlands.

Rakov, V. A., and M. A. Uman (2003), *Lightning: Physics and Effects*, 678 pp., Cambridge Univ. Press, Cambridge, UK.

Reynolds, S. E., M. Brook, and M. F. Gourley (1957), Thunderstorm charge separation, *J. Meteorol.*, *14*(5), 163–178.

Rutledge, S. A., E. R. Williams, and T. D. Keenan (1992), The down under Doppler and electricity experiment (DUNDEE): Overview and preliminary results, *Bull. Am. Meteorol. Soc.*, *73*(1), 3–16.

Sassen, K. (1987), Ice cloud content from radar reflectivity, *J. Clim. Appl. Meteorol.*, *26*(8), 1050–1053.

Sassen, K., and L. Liao (1996), Estimation of cloud content by W-band radar, *J. Appl. Meteorol.*, *35*(6), 932–938.

Saunders, C. P. R. (1993), A review of thunderstorm electrification processes, *J. Appl. Meteorol.*, *32*(4), 542–655.

Saunders, C. P. R., and I. M. Brooks (1992), The effects of high liquid water content on thunderstorm charging, *J. Geophys. Res.*, *97*(D13), 14,671–14,676.

Saunders, C. P. R., and S. L. Peck (1998), Laboratory studies of the influence of the rime accretion rate on charge transfer during crystal/graupel collisions, *J. Geophys. Res.*, *103*(D12), 13,949–13,956.

Saunders, C. P. R., W. D. Keith, and R. P. Mitzeva (1991), The effect of liquid water on thunderstorm charging, *J. Geophys. Res.*, *96*(D6), 11,007–11,017.

Saunders, C. P. R., H. Bax-Norman, C. Emersic, E. E. Avila, and N. E. Castellano (2006), Laboratory studies of the effect of cloud conditions on graupel/crystal charge transfer in thunderstorm electrification, *Q. J. R. Meteorol. Soc.*, *132*, 2653–2673, doi:10/1256/qj.05.218.

Schneider, T. L., and G. L. Stephens (1995), Theoretical aspects of modeling backscattering by cirrus ice particles at millimeter wavelengths, *J. Atmos. Sci.*, *52*(23), 4367–4385.

Shao, X. M., C. T. Rhodes, and D. N. Holden (1999), RF radiation observations of positive cloud-to-ground flashes, *J. Geophys. Res.*, *104*(D8), 9601–9608.

Sherwood, S. C., V. T. J. Phillips, and J. S. Wettlaufer (2006), Small ice crystals and the climatology of lightning, *Geophys. Res. Lett.*, *33*, L05804, doi:10.1029/2005GL025242.

Skamarock, W. C., J. G. Powers, M. Barth, J. E. Dye, T. Matejka, D. Bartels, K. Baumann, J. Stith, D. D. Parrish, and G. Hubler (2000), Numerical simulations of the July 10 Stratospheric-Tropospheric Experiment: Radiation, Aerosols, and Ozone/Deep Convection Experiment convective system: Kinematics and transport, *J. Geophys. Res.*, *105*(D15), 19,973–19,990.

Skamarock, W. C., J. E. Dye, E. Defer, M. C. Barth, J. L. Stith, B. A. Ridley, and K. Baumann (2003), Observational- and modeling-based budget of lightning-produced NOx in a continental thunderstorm, *J. Geophys. Res.*, *108*(D10), 4305, doi:10.1029/2002JD002163.

Skamarock, W. C., J. B. Klemp, J. Dudhia, D. Gill, D. Barker, W. Wang, and J. G. Powers (2005), A description of the Advanced Research WRF Version 2, *Tech. Note NCAR/TN-468+STR,* NCAR, Boulder, Colo.

Sun, J., and N. A. Crook (1997), Dynamical and microphysical retrieval from Doppler radar observations using a cloud model and its adjoint. part I: Model development and simulated data experiments, *J. Atmos. Sci.*, *55*(12), 835–852.

Sun, J., and N. A. Crook (2001), Real-time low-level wind and temperature analysis using single WSR-88D data, *Weather Forecast.*, *16*(1), 117–132.

Straka, J. M., D. S. Zrnic, and A. V. Ryshkov (2000), Bulk hydrometeor classification and quantification using polarimetric radar data: Synthesis of relations, *J. Appl. Meteorol.*, *39*(8), 1341–1372.

Takahashi, T. (1978), Riming electrification as a charge generation mechanism in thunderstorms, *J. Atmos. Sci.*, *35*(8), 1536–1548.

Takahashi, T., and K. Miyawaki (2002), Reexamination of riming electrification in a wind tunnel, *J. Atmos. Sci.*, *59*(5), 1018–1025.

Testud, J., W. Le Bouar, E. Obligis, and M. Ali-Mehenni (2000), The rain profiling algorithm applied to polarimetric weather radar, *J. Atmos. Oceanic. Technol.*, *17*(3), 332–356.

Thomas, R., P. Krehbiel, W. Rison, J. Harlin, T. Hamlin, and N. Campbell (2003), The LMA flash algorithm, in *Proceedings of the 12th, International Conference on Atmospheric Electricity, Versailles, France*, 9–13 June, pp. 655–656, ICAE.

Thomas, R., P. R. Krehbiel, W. Rison, S. J. Hunyady, W. P. Winn, T. Hamlin, and J. Harlin (2004), Accuracy of the lightning mapping array, *J. Geophys. Res.*, *109*, D14207, doi:10.1029/2004JD004549.

Thomason, J. W. G., A. J. Illingworth, and V. Marecal (1995), Density and size distribution of aggregating snow particles inferred from coincident aircraft and radar observation, in *Preprints of the 27th AMS Conference on Radar Meteorology, Vail, CO*, 9–13 October, pp. 127–128, *AMS*.

Vivekanandan, J., D. S. Zrnic, S. M. Ellis, R. Oye, A. V. Ryzhkov, and J. Straka (1999), Cloud microphysics retrieval using S-band dual-polarization radar measurements, *Bull. Am. Meteorol. Soc.*, *80*(3), 381–388.

Wicker, L. J., and W. C. Skamarock (2002), Time-splitting methods for elastic models using forward time schemes, *Mon. Weather Rev.*, *130*(8), 2088–2097.

Wiens, K. C., S. A. Rutledge, and S. A. Tessendorf (2005), The 29 June 2000 supercell observed during STEPS. part II: Lightning and charge structure, *J. Atmos. Sci.*, *62*(12), 4151–4177.

Williams, E. R. (1989), The tripole structure of thunderstorms, *J. Geophys. Res.*, *94*(D11), 13,151–13,167.

Williams, E. R. (2001), The electrification of severe storms. Severe Convective Storms, *Meteorol. Monogr.*, No. 50, AMS, 527–561.

Williams, E. R., and R. M. Lhermitte (1983), Radar tests of the precipitation hypothesis for thunderstorm electrification, *J. Geophys. Res.*, *88*(C15), 10,984–10,992.

Williams, E. R., R. Zhang, and J. Rydock (1991), Mixed-phase microphysics and cloud electrification, *J. Atmos. Sci.*, *48*(19), 2195–2203.

Witt, A., and S. P. Nelson (1991), The use of single-Doppler radar for estimating maximum hailstone size, *J. Appl. Meteorol.*, *30*(4), 425–431.

Workman, E. J., and S. E. Reynolds (1949), Electrical activity as related to thunderstorm cell growth, *Bull. Am. Meteorol. Soc.*, *30*, 142–149.

Yagi, T., and H. Uyeda (1980), Different size distributions of snow based on meteorological situations, in *Communications a la VIIIeme Conference International sur la Physique des Nuages*, pp. 231–234, Clermont-Ferrand, France.

Yuter, S. E., and R. A. Houze Jr. (1995), Three-dimensional kinematic and microphysical evolution of Florida cumulonimbus. part III: Vertical mass transport, mass divergence, and synthesis, *Mon. Weather Rev.*, *123*(7), 1964–1983.

Zrnic, D. S., A. Ryzhkov, J. Straka, Y. Liu, and J. Vivekanandan (2001), Testing a procedure for automatic classification of hydrometeor types, *J. Atmos. Oceanic Technol.*, *18*(6), 892–913.

H. J. Christian and W. A. Petersen, ESSC/NSSTC University of Alabama in Huntsville, 320 Sparkman Drive, Huntsville, AL 35699, USA. (hugh.chrsitian@nsstc.uah.edu; walt.petersen@nasa.gov)

W. Deierling, S. Ellis, and J. Latham, National Center for Atmospheric Research, P.O. Box 3000, Boulder, CO 80301, USA. (deierlin@ucar.edu; sellis@ucar.edu; latham@ucar.edu)